Environmental Science
Atmospheres

Accepted Manuscript

This article can be cited before page numbers have been issued, to do this please use: B. Killen, J. A. Fisher, C. S. Hansen, P. Krummel, M. K. Vollmer and S. Kable, *Environ. Sci.: Atmos.*, 2026, DOI: 10.1039/D6EA00034G.

ROYAL SOCIETY OF CHEMISTRY

rsc.li/esatmospheres

Environmental Significance Statement

View Article Online
DOI: 10.1039/D6EA00034G

Hydrofluoroolefins (HFOs) are replacing climate-warming hydrofluorocarbons (HFCs), but their environmental impacts remain uncertain. Using 3-D atmospheric modelling incorporating recent experimental findings, we provide a comprehensive assessment of global HFO-1234ze(E) degradation, including photochemical and deposition processes. Whilst HFO-1234ze(E) photochemistry produces the potent greenhouse gas HFC-23, the combined direct and indirect global warming potential of HFO-1234ze(E) (~13) remains far below regulatory thresholds and two orders of magnitude lower than the HFCs it replaces. We identify wet deposition of the intermediate trifluoroacetaldehyde (CF_3CHO) as a potentially significant source of trifluoroacetic acid (TFA), a persistent environmental contaminant. These findings confirm that HFO-1234ze(E) offers substantial climate benefits over traditional refrigerants whilst highlighting the need for TFA monitoring as HFO use increases.

View Article Online
DOI: 10.1039/D6EA00034G

Atmospheric fates and global warming potential of HFO-1234ze(E) and its degradation product trifluoroacetaldehyde (CF_3CHO)

Beth Killen[1], Jenny A. Fisher[2,3], Christopher S. Hansen[1], Paul B. Krummel[4], Martin K. Vollmer[5], and Scott H. Kable[1]

[1]School of Chemistry, UNSW Sydney, NSW 2052, Australia

[2]College of Science and Engineering, James Cook University, Douglas, QLD 4811, Australia

[3]Environmental Futures, University of Wollongong, Wollongong, NSW 2522, Australia

[4]CSIRO Environment, Aspendale, Victoria, Australia

[5]Laboratory for Air Pollution / Environmental Technology, Empa, Swiss Federal Laboratories for Materials Science and Technology, Überlandstrasse 129, 8600 Dübendorf, Switzerland

May 8, 2026

Abstract

Hydrofluoroolefins (HFOs) are replacing high-GWP hydrofluorocarbons (HFCs) across multiple applications including foam blowing, refrigeration, and aerosols, but their atmospheric degradation and climate consequences remain uncertain. We use the GEOS-Chem 3-D chemical transport model, supported by AtChem2 box-model simulations, to develop a complete representation of the atmospheric chemistry and fate of HFO-1234ze(E) and its key intermediate product, CF_3CHO. We focus on HFO-1234ze(E) as it is the dominant isomer in commercial use. The model includes newly measured CF_3CHO photolysis quantum yields to form fluoroform (HFC-23), the recently identified chemical pathways of HFO-1234ze(E) ozonolysis and CF_3CHO reversible reaction with HO_2, and explicit wet and dry deposition parameterisations. Using observationally constrained global HFO-1234ze(E) emissions of 15 Gg yr^{-1}, simulated HFO-1234ze(E) surface mixing ratios agree well with 2020-2024 observations at 8 Advanced Global Atmospheric Gases Experiment (AGAGE) network sites. We find that 99.6% of HFO-1234ze(E) is removed by reaction with OH, with the remaining 0.4% lost to ozonolysis. Sensitivity tests for effective Henry's law constants (K^*_H) spanning 10 - 10^6 M atm^{-1} show sensitivity of CF_3CHO fate to K^*_Hup to 10^4 M atm^{-1} and saturation at higher K^*_H Using an upper bound of 10^5 M atm^{-1}, deposition accounts for ≈51% of total CF_3CHO loss in GEOS-Chem (20% dry, 31% wet), with photolysis contributing ≈33% and OH reaction ≈15%. The reversible reaction with HO_2 contributes around 1% to net CF_3CHO loss due to rapid conversion of the reaction products back to reactants. We

View Article Online
DOI: 10.1039/D6EA00034G

calculate a total (direct + indirect) GWP_{100} for HFO-1234ze(E) of $11.4^{+3.1}_{1.9}$, with CF_3CHO photolysis to HFC-23 contributing $8.2^{+3.1}_{1.9}$. We also estimate a maximum potential formation of 4.5 Gg yr^{-1} of trifluoroacetic acid (TFA) under current emissions assuming complete conversion of wet-deposited CF_3CHO from HFO-1234ze(E), suggesting a potential unrecognised TFA source from all CF_3CHO sources.

View Article Online
DOI: 10.1039/D6EA00034G

1 Introduction

Fluorine-containing compounds have been a part of modern life for almost a century. Over recent decades, however, they have received significant attention in scientific and popular media for their environmental persistence and unintended consequences. Industrial fluorine-containing gases have been used for a multitude of purposes, including air conditioning, heat pumps, refrigeration, foam-blowing agents and insulation materials. In 1987, the Montreal Protocol initiated the phase-out of first- and second-generation refrigerants (chlorofluorocarbons, CFCs, and hydrochlorofluorocarbons, HCFCs) (1) after these substances were found to significantly deplete the ozone layer, increasing exposure to ultraviolet radiation at the Earth's surface. In 2016, the Kigali Amendment to the Montreal Protocol stipulated the phase out of the third-generation refrigerants (hydrofluorocarbons, HFCs) (2), which do not deplete the ozone layer but are potent greenhouse gases with high Global Warming Potential (GWP).

The search for alternatives to high-GWP gases led to the development of hydrofluoroolefins (HFOs). HFOs are similar to HFCs, except that they possess a carbon-carbon double bond, making them prone to oxidation by hydroxyl (OH) radicals in the troposphere. This reactivity results in shorter atmospheric lifetimes and is the reason HFOs are generally considered to have low GWP, making them appealing as climate-friendly refrigerants (3). However, the environmental impact of HFOs depends on the fate of their atmospheric degradation products. Several HFOs, including HFO-1234yf, HFO-1225ye(Z) and HFO-1225ye(E) degrade to trifluoroacetic acid (TFA), a persistent compound in aquatic environments (4). HFO-1234ze(E), HFO-1336mzz and HCFO-1233zd degrade to trifluoroacetaldehyde (CF_3CHO) (5). CF_3CHO is of particular concern because it can photolyse to form fluoroform (CHF_3, widely known as HFC-23), a potent greenhouse gas.

We focus in this work on HFO-1234ze(E) (1,3,3,3-tetrafluoropropene), a widely used HFC replacement compound that produces CF_3CHO via its dominant atmospheric removal pathway, reaction with OH (6), and also directly produces HFC-23 via ozonolysis (7). HFO-1234ze(E) is already in widespread use, with its use set to increase as HFCs are rapidly phased down (8). HFO-1234ze(E) was originally developed for foam blowing applications (particularly in extruded polystyrene and polyurethane foams) but is also used in refrigeration, air conditioning (including chillers and heat pumps), and as an aerosol propellant.

A summary of the currently understood atmospheric chemistry of HFO-1234ze(E) is shown in Fig. 1. Reaction with the OH radical leads to the formation of trifluoroacetaldehyde, CF_3CHO:

$$\text{HFO-1234ze(E)} + \text{OH} \rightarrow CF_3CHO + \text{CHFO} \quad \text{(R1)}$$

while reaction with ozone leads directly to HFC-23 formation:

$$\text{HFO-1234ze(E)} + O_3 \rightarrow \text{HFC-23} + \text{CHFO} + CO_2 \quad \text{(R2)}$$

View Article Online
DOI: 10.1039/D6EA00034G

The end-products of R2 are CO_2 and HFC-23, plus CHFO, which decomposes to HF + CO. While CO_2 and HFC-23 are greenhouse gases, HF and CO are not persistent in the atmosphere. R1 also forms CHFO, along with CF_3CHO that undergoes its own series of atmospheric reactions, including reaction with OH and photolysis:

$$CF_3CHO + OH \rightarrow CF_3CO + H_2O \quad (R3)$$

$$CF_3CHO + h\nu \rightarrow CF_3 + HCO \quad (R4)$$

$$CF_3CHO + h\nu \rightarrow HFC\text{-}23 + CO \quad (R5)$$

The CF_3 radical produced from R4 reacts rapidly with O_2 under atmospheric conditions to form CF_3O_2, which undergoes further oxidation to produce COF_2 (carbonyl fluoride) and ultimately CO_2 and HF (9–11). The CF_3CO radical produced from R3 either decomposes to give CF_3 and CO_2, or reacts with O_2 to form the CF_3CO_2 peroxy radical, which subsequently decomposes to yield CF_3 and CO_2 (12). Neither pathway produces HFC-23.

Recently, a computational chemistry study (13) proposed that CF_3CHO also reacts facilely with the HO_2 radical in a reversible reaction:

$$CF_3CHO + HO_2 \rightleftharpoons CF_3CH(OH)OO \quad (R6)$$

However, that study did not evaluate whether the reverse reaction limits the atmospheric significance of this pathway. If R6 represents a significant CF_3CHO sink, it would reduce photolytic production of HFC-23 via R5 and affect the total climate impact of HFO-1234ze(E).

HFC-23 is a very strong greenhouse gas with a 100-year GWP_{100} = 14,600 (14), and therefore the production of HFC-23 from R2 and R5 has significant implications for assessing the climate impact of HFO-1234ze(E). The rate coefficient for R2 was published recently by McGillen *et al.* (7), but historical values for the quantum yield of R5 have varied by orders of magnitude. The earliest results by Dodd *et al.* used 313 nm radiation and reported quantum yields of φ_5 = 2.1% (15). Subsequent studies by Pearce *et al.* found no evidence of φ_5 at 313 nm (16). More recent results from Sulbaek Andersen and Nielsen (17) also did not detect formation of HFC-23 across pressures ranging from 100-700 Torr. Two recent papers provide consistent results for wavelength- and pressure-dependent quantum yields for R4 and R5. In 2024, Thomson *et al.* (18) reported quantum yields for R4 and R5 at 308 nm for pressures from 75 to 750 Torr, including φ_5 (750 Torr) = 0.023%. Shortly thereafter, Van Hoomissen *et al.* (19) reported pressure-dependent quantum yields for φ_4 and φ_5 at 248, 266, 281 and 308 nm at 100 and 650 Torr, including φ_5 = 0.0302% at 308 nm and 650 Torr. The pressure dependence of φ_5 means that HFC-23 yields will vary with altitude, requiring a 3-D model to quantify the atmospheric implications.

View Article Online
DOI: 10.1039/D6EA00034G

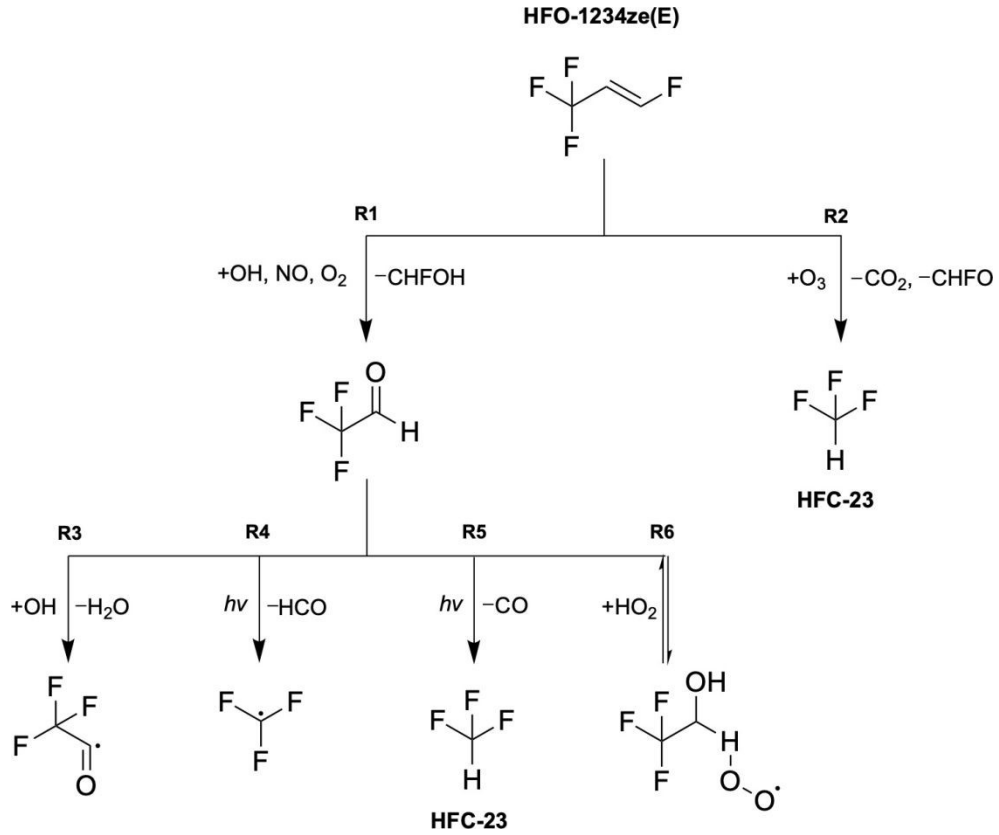

Figure 1: Proposed atmospheric degradation pathway of HFO-1234ze(E) and CF_3CHO to form HFC-23. The Criegee intermediate from ozonolysis reaction R2 decomposes to form HFC-23 with a yield of 7.9%, along with CO_2 and CHFO (20). HFC-23 is also produced via minor channel photolysis of CF_3CHO, with yield as discussed in the text.

In addition to chemical loss mechanisms, summarised as R1 - R6, atmospheric species can be physically removed via wet and dry deposition. Wet and dry deposition can be important sinks for water-soluble species, with the efficiency of uptake into cloud droplets and precipitation governed by the effective Henry's Law constant, K^*_H. HFO-1234ze(E) has a low water solubility of 0.373 g L^{-1} at 20 °C, and thus is not considered to undergo deposition, consistent with treatment in previous modelling studies (21–23). Deposition of the CF_3CHO intermediate, however, is the subject of ongoing debate.

The K^*_H for CF_3CHO has not been reported. Pérez-Peña *et al.* (5) were the first to incorporate its deposition in model simulations, parameterising combined wet and dry depositional losses through a single loss constant. Their simulations revealed that even with conservative solubility assumptions, deposition could reduce the CF_3CHO atmospheric lifetime by 20-40%, thus altering its distribution between atmospheric and surface reservoirs. Their analysis suggested that deposition can play a significant role in CF_3CHO loss, although the magnitude of this effect depends on K^*_H assumptions. The fate of CF_3CHO is particularly

View Article Online
DOI: 10.1039/D6EA00034G

important because deposition represents a pathway to TFA formation (via hydrolysis of deposited CF_3CHO) while simultaneously reducing photolytic HFC-23 production via R5. Nielsen *et al.* (24) argued that the values of K^*_H chosen by Pérez-Peña *et al.* were too small and that if the solubility of CF_3CHO mirrored its chlorinated analogue, deposition would become the dominant mechanism controlling CF_3CHO's atmospheric fate. Using a lifetime-based estimate, Pérez-Peña *et al.* (25) showed that CF_3CHO loss to deposition was only moderately sensitive to K^*_H, changing by a factor of 2.5 in response to a three-order-of-magnitude increase in K^*_H. Both authors highlighted the need to explore the atmospheric implications of a higher K^*_H as essential for understanding the atmospheric fate of CF_3CHO.

Modelling of the atmospheric fate of HFO-1234ze(E) has not kept pace with the rapid evolution of new chemistry concerning HFO-1234ze(E), including accurate quantum yields for R4 and R5, ozonolysis rate coefficient for R2, and the recent identification of reversible reaction of CF_3CHO with HO_2 (R6). This has left a number of unanswered questions, including *i)* what is the overall yield of the strong greenhouse gas, HFC-23, when both ozonolysis (R2) and photochemistry (R5) are included, *ii)* what is the impact of HO_2 chemistry, R6, which was reported to have a faster rate coefficient than the OH reaction (R1); *iii)* what is the sensitivity of the atmospheric fate of CF_3CHO to reasonable values of K^*_H; and *iv*) considering the above, what is the final distribution of fates for HFO-1234ze(E) and its resultant indirect GWP? Answering those questions requires integrating spatial and temporal variability in emissions, photolytic and chemical reaction rates, and deposition.

In this work, we incorporate all these new advances to develop a comprehensive simulation of the atmospheric chemistry of HFO-1234ze(E) and its main degradation product CF_3CHO in a global 3-D chemical transport model (GEOS-Chem). We first use a box model (AtChem2) to evaluate the importance of the reversible reaction between CF_3CHO and HO_2. We then test the sensitivity of CF_3CHO depositional losses to K^*_H. Using the results from these initial studies, we implement all relevant reactions and processes in GEOS-Chem, which we use to quantify the fate of HFO-1234ze(E) and its total GWP including indirect impact through HFC-23 production.

2 Model Configuration

We use two models in this work: the AtChem2 0D box model incorporating the Master Chemical Mechanism (AtChem2-MCMv3.3.1) and the GEOS-Chem 3-D global chemical transport model. In Section 2.1, we outline the setup and implementation of the AtChem2-MCMv3.3.1 simulations used to test the reaction between CF_3CHO and HO_2. In Section 2.2, we describe the GEOS-Chem model configuration, including the new emissions (Section 2.2.1), chemical mechanism (Section 2.2.2), and deposition parameters (Section 2.2.3) required to implement the HFO-1234ze(E) → CF_3CHO → HFC-23 chemical cascade.

View Article Online
DOI: 10.1039/D6EA00034G

2.1 Implementation of HFO-1234ze(E) chemistry in the AtChem2-MCMv3.3.1 box model

We first test the relative importance of the $CF_3CHO+HO_2$ reaction to total CF_3CHO loss using the AtChem2 box model implementing the Master Chemical Mechanism (MCM) v3.3.1, a near-explicit chemical mechanism describing detailed gas-phase oxidation in the troposphere. The current version of the MCM includes 17,224 reactions and 5,832 species. It does not currently contain any HFO species or chemistry. Table 1 summarises the new reactions added to the MCM. Both HFO-1234ze(E) and CF_3CHO have well-characterised reactions with the OH radical (R1 and R3, respectively). The reaction between CF_3CHO and HO_2 (R6) yields a hydroxy-peroxy radical ($CF_3CH(OH)OO$). This reaction is reversible, and the reverse reaction (R6') was also added to the MCM (13). We also added removal of the $CF_3CH(OH)OO$ radical by reaction with NO (R7) (13). As these simulations were designed solely to determine the relative contribution of the HO_2 reaction (R6) to total CF_3CHO loss, we did not separate the two photolysis channels but rather used the total photolysis quantum yield from Chiappero et al. (R8). For the same reason, we did not include the reaction between HFO-1234ze(E) and O_3.

Table 1: Reactions and corresponding rate coefficients at 298 K added to the MCMv3.3.1. All rate coefficients are in units of cm^3 $molec^{-1}$ s^{-1} except R6′ (marked with †), which has a unit of s^{-1}.

No.	Reaction	Rate Coefficient	Quantum Yield
R1	HFO-1234ze(E) + OH → CF_3CHO + CHFO	7.06×10^{-13} [a]	
R3	CF_3CHO + OH → CF_3CO + H_2O	5.80×10^{-13} [b]	
R6	CF_3CHO + HO_2 → $CF_3CH(OH)OO$	2.80×10^{-13} [c]	
R6′	$CF_3CH(OH)OO$ → CF_3CHO + HO_2	9.71×10^{2} [c] †	
R7	$CF_3CH(OH)OO$ + NO → $CF_3CH(OH)O$ + NO_2	1.5×10^{-11} [c]	
R8	CF_3CHO + $h\nu$ → Products		0.17 [d]

[a] Antiñolo *et al.* (26), [b] Calvert *et al.* (27), [c] Long *et al.* (13), [d] Chiappero *et al.* (28)

We constrain the box model using surface observations from the July-August 2012 ClearfLo (Clean Air for London) measurement campaign to represent a typical urban environment (29), with a fixed temperature of 298 K. We therefore consider this simulation indicative of surface-level conditions in Northern Hemisphere summer. This is a limitation of the box model simulation, as reaction with HO_2 may become more significant at higher altitudes, which are characterised by lower temperatures and pressures. More realistic temporal, spatial and meteorological variability are explored in the subsequent simulations using the global model.

View Article Online
DOI: 10.1039/D6EA00034G

2.2 Implementation of HFO-1234ze(E) simulation in GEOS-Chem

GEOS-Chem is a widely used global 3D atmospheric chemical transport model (30) driven by assimilated meteorology from the NASA Global Modelling and Assimilation Office (GMAO) Goddard Earth Observing System (GEOS). GEOS-Chem does not currently include an HFO simulation capability. Here, we started from GEOS-Chem Classic version 14.3.0 and modified it to include all known chemical and physical processes associated with HFO-1234ze(E) and CF_3CHO. The simulations were driven by Modern-Era Retrospective Analysis for Research and Applications, Version 2 (MERRA-2) meteorology. The native horizontal resolution of MERRA-2 (0.5° x 0.667°) was downgraded to 4° x 5° for computational efficiency, with 72 vertical layers. Standard global full-chemistry simulations were run for a one-year period from 01 January 2019 to 31 December 2019 following a six-month spin-up, which is sufficient to equilibrate the short-lived species in this study (HFO-1234ze(E), ~16 days; CF_3CHO, ~2 days). These chemical lifetimes are many orders of magnitude longer than typical boundary layer turbulent mixing timescales, ensuring that both species are well-mixed within model grid boxes before significant chemical conversion occurs. This is a standard assumption in global chemical transport models (31, 32). In GEOS-Chem, sub-grid scale transport is driven by meteorological fields from the NASA GMAO, which include parameterised boundary layer mixing and convective transport (33). Note that we do not simulate HFC-23 in this work; instead, we calculate HFC-23 production from HFO-1234ze(E), directly and via the CF_3CHO intermediate.

2.2.1 Emissions

GEOS-Chem calculates emissions using the Harmonised Emissions Component (HEMCO) software (34). For non-HFO emissions, our simulations used anthropogenic emissions from the Community Emissions Data System (CEDS) inventory (35), biomass burning emissions from the Global Fire Emissions Database version 4 (GFED4) inventory (36) and biogenic VOC emissions from the Model of Emissions of Gases and Aerosols from Nature version 2.1 (MEGAN v.2.1) inventory (37).

We added two different estimates of gridded HFO-1234ze(E) emissions into HEMCO: a hypothetical China-only HCFC-141b replacement scenario used previously by Wang *et al.* (8) and Pérez-Peña *et al.* (5), and a more realistic global emissions scenario developed in this work. We used the hypothetical China-only emissions for Henry's law sensitivity tests (Section 3.2), and the global emissions for all other simulations (Section 3.3). The two emission inventories are described in the following sub-sections.

2.2.1.1 HFO-1234ze(E) as a replacement for HCFC-141b in China Two previous modelling studies have examined the degradation of HFO-1234ze(E) using the emissions scenario described in Wang *et al.* (5, 8). In that scenario, Wang *et al.* assume complete replacement of HCFC-141b with HFO-1234ze(E), one of its proposed replacements, on a 1:1 mass basis (8). HCFC-141b was developed as an interim compound during the phase down of CFCs, and its production has been gradually phased out since 2003 (38).

View Article Online
DOI: 10.1039/D6EA00034G

As the emissions inventory developed by Wang *et al.* is not publicly available, we reproduced a variant for this work. Gridded emissions of HFO-1234ze(E) over China were generated as input for the HEMCO emissions component in GEOS-Chem. A total annual emission of 12.6 Gg yr^{-1} was implemented, matching Wang *et al.* (8). The geographical distribution of emissions within China was modelled using 2015 population density data as a proxy (see Figure S1 for population density map) (39). The resulting China emissions inventory is shown in Figure 2c.

2.2.1.2 Observationally constrained global HFO-1234ze(E) emissions estimate To better represent the distribution of HFO emissions beyond China, we developed a global emissions inventory through an iterative approach combining literature estimates with observational constraints. We start with an initial constraint implied by a 2024 Montreal Protocol Scientific Assessment Panel (SAP) report that estimates ~150 tonnes per year of HFC-23 would be produced from HFO-1234ze(E) degradation (40). Based on the assumptions detailed in that report (100% conversion of HFO-1234ze(E) to CF_3CHO; fractional loss of CF_3CHO to photolysis, $Y_{\text{photolysis}}$ = 0.75; HFC-23 yield from CF_3CHO photolysis, $a_{\text{photolysis}}$ = 0.003) we estimate approximately 110 Gg HFO-1234ze(E) emitted annually as follows:

$$E_{\text{HFO-1234ze(E)}} = \frac{P_{\text{HFC-23}}}{a_{\text{photolysis}} \times Y_{\text{HFC-23}} \times \frac{M_{\text{HFC-23}}}{M_{\text{HFO-1234ze(E)}}}}$$

where $P_{\text{HFC-23}}$ is the estimated mass of HFC-23 produced from HFO-1234ze(E), $M_{\text{HFC-23}}$ is the molar mass of HFC-23 and $M_{\text{HFO-1234ze(E)}}$ is the molar mass of HFO-1234ze(E). The SAP report acknowledges this likely overestimates global emissions as it extrapolates from limited European measurements, and because 0.003 is an upper limit for HFC-23 formation from CF_3CHO (40) (41).

We tested this 110 Gg yr^{-1} estimate in GEOS-Chem and compared modelled surface mixing ratios against preliminary 2020 Advanced Global Atmospheric Gases Experiment (AGAGE) observations from two European monitoring sites (42) (Dübendorf and Jungfraujoch, both in Switzerland). The model overestimated observations at these sites by a factor of approximately 7, suggesting true emissions are lower. Assuming linearity between emissions and mixing ratios, we scaled the global emissions inventory by this ratio, resulting in total global emissions of 15 Gg yr^{-1} (approximately 14% of the SAP-derived upper bound). Subsequently released AGAGE data from additional monitoring sites (43) provided independent validation of this emission estimate, as detailed in Section 3.3.1. We spatially distributed these emissions using the 0.1° x 0.1° EDGAR 2018 HFC-134a emissions (44) as a proxy. We selected 2018 (pre Kigali Amendment implementation) HFC emissions because HFO-1234ze(E) is being adopted as a replacement for HFCs in the same applications and geographic regions. While HFO-1234ze(E) was originally developed primarily for foam blowing applications, it is also used in refrigeration and air conditioning systems. HFC-134a serves these same multiple applications,

View Article Online
DOI: 10.1039/D6EA00034G

making it an appropriate spatial proxy from combined end uses of HFO-1234ze(E), in the absence of bottom-up HFO-1234ze(E) emission inventories.

Figure 2a shows the final global distribution of HFO-1234ze(E) emissions used in the GEOS-Chem simulations. The figure also compares emissions over China in the global inventory (regridded to 1° x 1° for comparison; Figure 2b) to those in the hypothetical replacement inventory (Section 2.2.1.2; Figure 2c). In the global scenario, annual emissions over China are 3.9 Gg yr^{-1}. This suggests that the 12.6 Gg yr^{-1} derived by Wang *et al.* (8) from full replacement of 2015 HCFC-141b emissions is likely too high. However, without HFO-1234ze(E) observations in China or downwind regions, it is impossible to quantitatively evaluate either estimate.

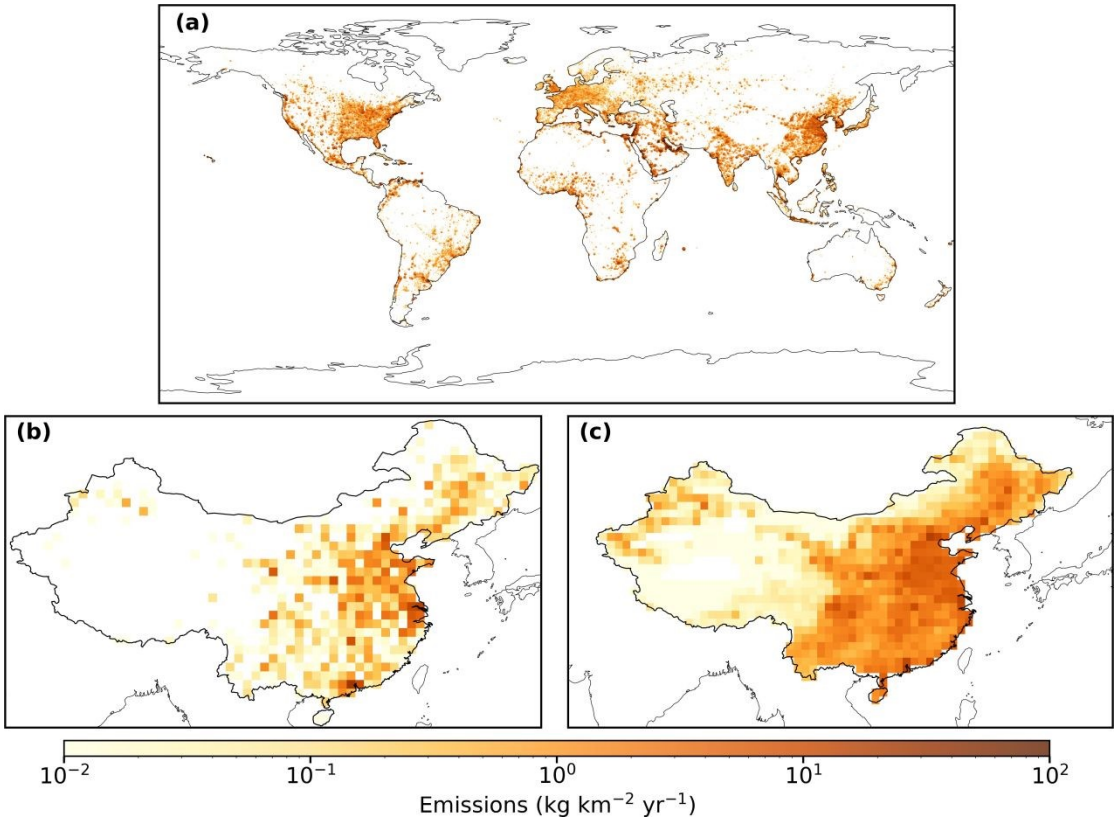

Figure 2: HFO-1234ze(E) emission scenarios used in GEOS-Chem (see text for details). a) Global baseline scenario (0.1° × 0.1°), total = 15 Gg yr^{-1}. b) China subset from panel (a) regridded to 1° × 1°, regional total = 3.9 Gg yr^{-1}. c) Alternative China scenario (1° × 1°), after Wang *et al.* (8), regional total = 12.6 Gg yr^{-1}.

View Article Online
DOI: 10.1039/D6EA00034G

2.2.2 Chemistry

GEOS-Chem implements the Cloud-J photolysis code for calculation of photolysis rates from quantum yield and absorption cross section data (45). We used absorption cross sections from Table 4E-27 of the JPL Data Evaluation No. 19-5 (46). For quantum yields, we adopted φ_4 from the JPL data evaluation (46) and φ_5 measured by Van Hoomissen *et al.* (19), including their pressure dependence, and interpolated these values to 1 nm resolution. The original values for φ_5 from Van Hoomissen *et al.* and the interpolated values are reported as Supplementary Information (Table S1). For wavelengths beyond the range of available measurements (>320 nm), we set $\varphi_4 = \varphi_5 = 0$ as a boundary condition, following the decreasing trend observed in the measured quantum yield data. The original 1-nm cross section data are then grouped into 18 wavelength bins of varying widths spanning 177–778 nm. Within each bin, Cloud-J integrates the cross sections, quantum yields and actinic flux to calculate photolysis rates (J-values), which are used in GEOS-Chem to represent photochemical loss in the troposphere and stratosphere.

The new reactions implemented into the model along with their corresponding rate constants are detailed in Table 2. These are largely the same as those used in AtChem-MCM (Table 1), but with the addition of temperature dependence (R1, R3, R6), separating the two photolysis channels (R4, R5), and ozonolysis of HFO-1234ze(E) (R2). These are implemented in GEOS-Chem via the Kinetic PreProcessor (KPP) used to solve chemical kinetics (47).

2.2.3 Deposition

We include dry and wet deposition of CF_3CHO. GEOS-Chem parameterises dry deposition using a resistance-in-series model (49) and wet deposition as described by Liu *et al.* (50). Both parameterisations depend on the effective Henry's Law Constant, K^*_H, which is currently unknown for CF_3CHO. Pérez-Peña *et al.* used a value of 13.17 M atm^{-1} by analogy to the hydrogenated analogue CH_3CHO (5), while Nielsen *et al.* suggested K^*_H would be closer to the chlorinated equivalent value of 3.44×10^5 M atm^{-1} (24). We therefore performed sensitivity tests using K^*_H values ranging from 10 to 10^6 M atm^{-1}, spanning the estimates proposed in recent literature to constrain the impact of the uncertainty of K^*_H on the atmospheric chemistry of CF_3CHO.

The dry deposition parameterisation also depends on a reactivity factor, f_0, which has not been measured for CF_3CHO. Pérez-Peña *et al.* (5) found that there was limited sensitivity to the choice of f_0. Following Pérez-Peña *et al.* (5), we use $f_0 = 1$ for our simulations.

3 Results and discussion

3.1 Box Model Evaluation of $CF_3CHO + HO_2$ Reaction

We first use the AtChem-MCM box model to evaluate the relative contribution of reaction with HO_2 to total photochemical loss of CF_3CHO. Figure 3 shows the relative importance of each CF_3CHO photochemical

View Article Online
DOI: 10.1039/D6EA00034G

Table 2: New reactions and corresponding rate coefficients added to GEOS-Chem. Rate constants are given at 298 K unless temperature dependence is specified. All rate coefficients are in units of cm^3 $molec^{-1}$ s^{-1} except R6′ (marked with †), which has a unit of s^{-1}.

No.	Reaction	Rate Coefficient, k	Quantum Yield, φ
R1	HFO-1234ze(E) + OH → CF_3CHO + CHFO	$7.6 \times 10^{-13} \left(\frac{T}{298}\right)^{2.44} \exp\left(\frac{666}{T}\right)$ [a]	
R2	HFO-1234ze(E) + O_3 → HFC-23 + CHFO + CO_2	2.44×10^{-21} [b]	
R3	CF_3CHO + OH → CF_3CO + H_2O	$3.8 \times 10^{-13} \left(\frac{T}{300}\right)^{2} \exp\left(\frac{131}{T}\right)$ [c]	
R4	CF_3CHO + $h\nu$ → CF_3 + HCO		see Table S1 [e]
R5	CF_3CHO + $h\nu$ → HFC-23 + CO		see Table S1 [f]
R6	CF_3CHO + HO_2 → $CF_3CH(OH)OO$	$8.88 \times 10^{-16} \exp\left[\frac{1723}{T}\right]$ [d]	
R6′	$CF_3CH(OH)OO$ → CF_3CHO + HO_2	$2.29 \times 10^{14} \exp\left[\frac{-7621}{T}\right]$ [d] †	
R7	$CF_3CH(OH)OO$ + NO → $CF_3CH(OH)O$ + NO_2	1.5×10^{-11} [d]	

[a] Antiñolo *et al.* (26), [b] McGillen *et al.* (7), [c] Baumann *et al.* (48), [d] Long *et al.* (13), [e] JPL Data Evaluation 19-5 (46), [f] Van Hoomissen *et al.* (19)

loss process as simulated by the box model. In Figure 3a, we show the results when the box model includes the forward reaction (R6, CF_3CHO + HO_2) but does not include the reverse reaction (R6′, $CF_3CH(OH)OO$ decomposition). In this scenario, reaction with HO_2 is the dominant sink for CF_3CHO. However, when the reverse reaction is introduced, as shown in Figure 3b, reaction with HO_2 becomes negligible, accounting for 0.1% of total photochemical loss of CF_3CHO. CF_3CHO loss is dominated by photolysis (≈80%), followed by reaction with OH (≈20%). This result highlights that although almost 80% of CF_3CHO is initially removed via reaction with HO_2, the resulting radical is unstable and rapidly decomposes back to CF_3CHO and HO_2 before it can react further, and thus the net effect is almost zero. We note that these simulations include chemical losses only. When deposition is included, the overall contribution of reaction with HO_2 to total CF_3CHO is reduced further.

To account for uncertainties, we tested the sensitivity of our results to different conditions, independently increasing the HO_2 mixing ratio and the forward reaction rate by a factor of 10 each. We also performed box model simulations representative of conditions at around 5 km altitude where the pressure-dependent reaction is more favorable. The results from these simulations are presented in Figure S2 in the Supplementary Information. In all scenarios, CF_3CHO loss to reaction with HO_2 remained under 4%. Our results indicate

View Article Online
DOI: 10.1039/D6EA00034G

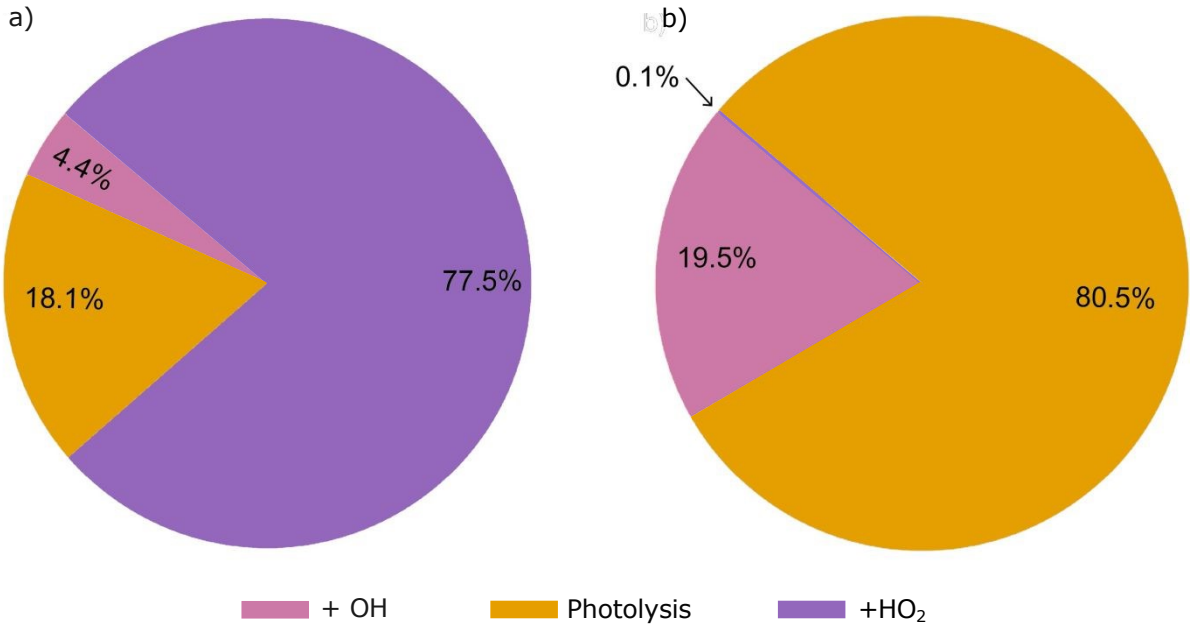

Figure 3: Percentage contribution of each of the photochemical loss processes to the total photochemical loss of CF_3CHO derived from the AtChem2 box model simulations using the modified MCMv3.3.1 with a) excluding the reverse reaction (R6′) and b) including the reverse reaction (R6′).

that the reaction is unlikely to dominate under tropospheric conditions, contrary to the findings of the original study (13).

3.2 Sensitivity of CF_3CHO fate to Henry's Law Constant

Given the uncertainty of $K^*_H(CF_3CHO)$ and its implication for depositional losses, we performed a series of sensitivity tests in GEOS-Chem, using K^*_H = 10, 10^2, 10^3, 10^4, 10^5, and 10^6 M atm^{-1} as input to both the dry and wet deposition schemes. These values were tested during a northern hemisphere winter month (January) and a summer month (July). For these simulations, we used the simulation with HFO-1234ze(E) emissions over China only as described in Section 2.2.1.1. This allows us to compare the results with those of Pérez-Peña *et al.* (5), who used the same emissions data.

Figure 4 shows a linear-log plot of the wet, dry and total deposition fluxes as a function of K^*_H in both January (Figure 4a) and July (Figure 4b). Wet deposition loss increases approximately linearly with $\log(K^*_H)$ between K^*_H = 10 and 10^4 M atm^{-1}, evincing a logarithmic relationship between deposition loss and K^*_H over this range. For $K^*_H > 10^4$ M atm^{-1}, the curve flattens, and loss remains constant for $K^*_H > 10^5$ M atm^{-1}. Previous studies have also shown that wet deposition contributions typically increase with K^*_H until around

View Article Online
DOI: 10.1039/D6EA00034G

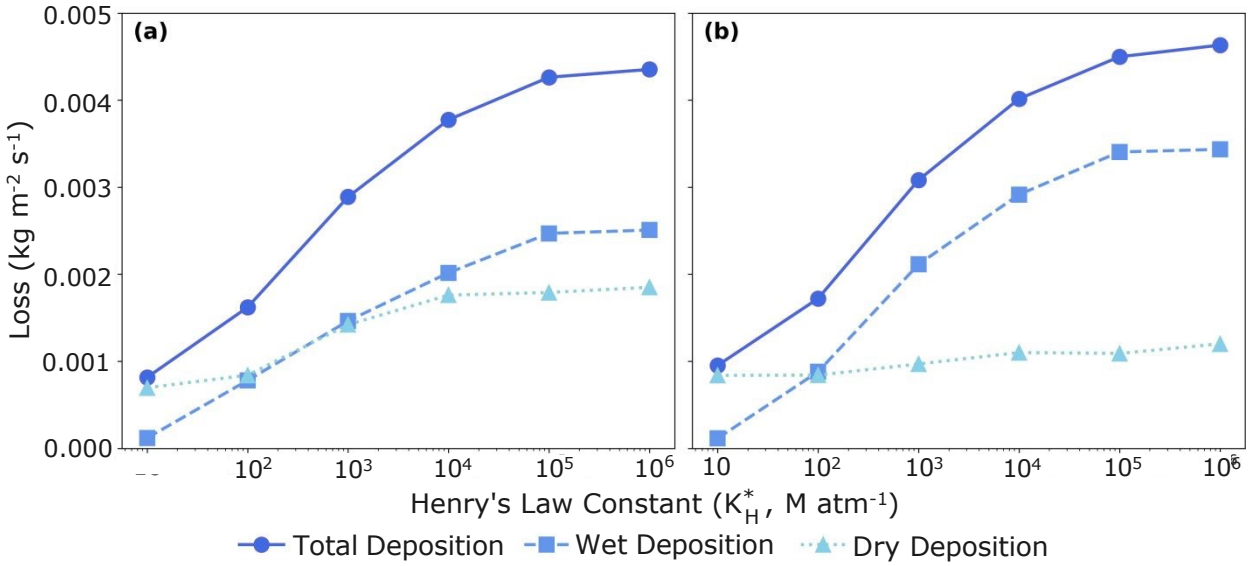

Figure 4: Wet (blue squares), dry (light blue triangles), and total (dark blue circles) deposition (kg m^{-2} s^{-1}) in a) January and b) July as a function of K^*_H

10^5 M atm^{-1}, where the efficiency of wet deposition peaks and the process becomes saturated (51). This saturation occurs because at sufficiently high K^*_H, the dissolution process becomes so thermodynamically favourable that every collision between a gas phase molecule and an aerosol droplet results in uptake. At this point, the wet deposition rate is limited by the rate of diffusion across droplet surfaces rather than by K^*_H (51). The saturation behaviour is consistent in both January and July. The difference in the magnitude of the wet deposition fluxes between the two months can be attributed to rainfall frequency and intensity, which are typically much higher in July (52).

Figure 4 also shows how the dry deposition flux varies with K^*_H in the two months tested. K^*_H has much less effect on dry deposition, primarily affecting the non-stomatal pathway by affecting leaf cuticle resistance (49). Higher K^*_H values increase the solubility of the species at the leaf surface, enhancing non-stomatal deposition. However, since stomatal deposition remains largely unaffected by changes in K^*_H, dry deposition is much less sensitive to changes in K^*_H than wet deposition. Dry deposition flux rates are higher in winter months when temperatures are lower (53). This is primarily due to the influence of temperature on the stomata of plants. Higher temperatures cause the plant stomata to close, thus reducing the surface area available for gas exchange (54). Overall, the total (wet plus dry) depositional loss is relatively invariant between the two months, with more wet deposition in July largely balanced by more dry deposition in January.

We use the sensitivity tests to assess the impact of K^*_H on the fate of CF_3CHO. Figure 5 illustrates the seasonal competition between photochemical and depositional loss processes, showing the fractional

View Article Online
DOI: 10.1039/D6EA00034G

contribution of each loss process to total CF_3CHO removal. In January (Figure 5a), photochemical loss dominates up to K^*_H = 10^3 M atm^{-1} and deposition dominates at higher K^*_H In contrast, in July (Figure 5b), deposition never exceeds photochemical loss. While summer conditions enhance deposition rates, increased sunlight hours also increase the photolysis rate and OH reactivity. We find that from K^*_H = 10^5 M atm^{-1}, the fractional loss to deposition saturates at ~60% in January (35% wet, 25% dry) and ~45% in July (35% wet, 11% dry).

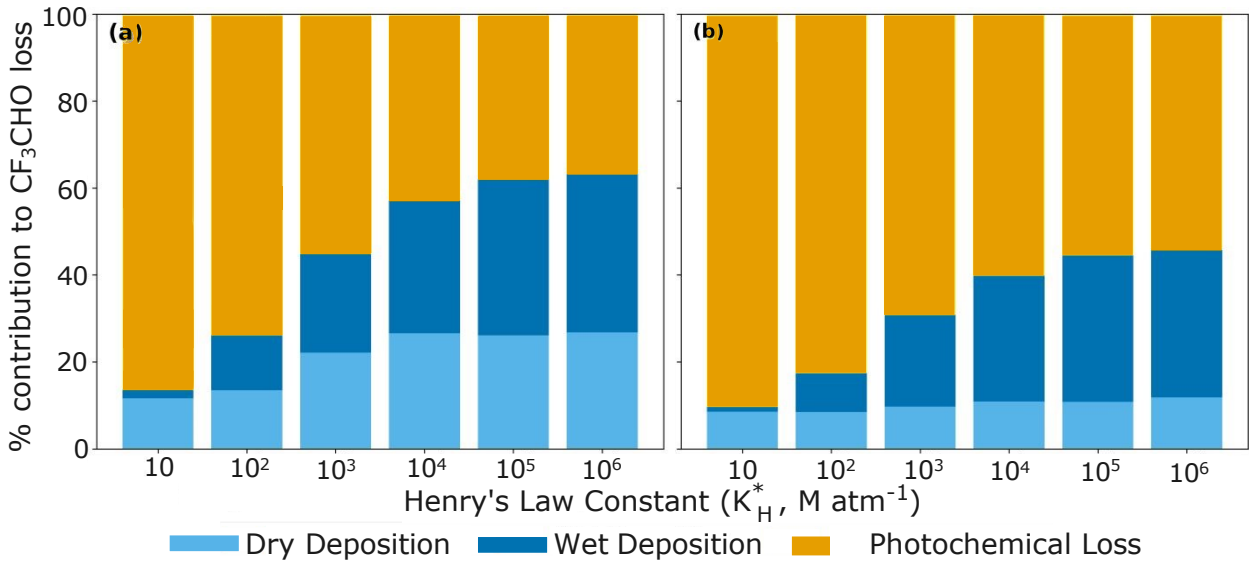

Figure 5: Relative contributions of dry deposition, wet deposition and photochemical loss to total CF_3CHO removal as a function of K^*_H in a) January and b) July.

K^*_H for CF_3CHO has not been measured experimentally. Previous work has posited a value of 3.3 ×10^4 M atm^{-1} or higher, based on scaling of its chlorinated analogue (24). Based on this proposed value combined with our sensitivity analysis showing near-saturation behaviour from 10^5 M atm^{-1} (Figures 4 and 5), we use K^*_H = 10^5 in subsequent simulations as indicative of the upper end of the plausible range.

3.3 Global atmospheric modelling of HFO-1234ze(E) chemistry

We performed a 1-year global simulation using GEOS-Chem to evaluate the atmospheric implications of 15 Gg yr^{-1} of HFO-1234ze(E) emissions. In this section, we first evaluate the model's performance against surface observations of HFO-1234ze(E) to assess how well it captures observed spatial gradients and seasonal cycles, analysing the discrepancies to identify potential limitations in our emission assumptions (Section 3.3.1). We then quantify CF_3CHO and HFC-23 production from the model (Section 3.3.2 and 3.3.3). Finally, we evaluate the contribution of HFC-23 formation to the indirect GWP_{100} of HFO-1234ze(E) and estimate how this process may contribute to the observed annual increase of 1 ppt of atmospheric HFC-23 (Section 3.3.3).

View Article Online
DOI: 10.1039/D6EA00034G

3.3.1 HFO-1234ze(E) distribution and model evaluation

We evaluated the modelled HFO-1234ze(E) surface mixing ratios using AGAGE measurements reported by Vollmer *et al.* (43). We selected 8 measurement sites that span diverse regional environments and are far enough from emission sources to be representative of the well-mixed coarse model grid boxes. Six sites are located in the Northern Hemisphere: Zeppelin, Mace Head, Jungfraujoch, Trinidad Head, Gosan and Ragged Point. Two sites are in the Southern Hemisphere: Cape Matatula and Kennaook/Cape Grim (55). The sites are represented in Figure 6a as circles, annotated by the first letter of the site name. Mace Head, Trinidad Head, Cape Matatula, Ragged Point and Kennaook/Cape Grim are coastal stations that primarily sample clean marine boundary layer air for most of the year, and are therefore broadly representative of background atmospheric conditions (56). Jungfraujoch is a high-altitude site in the Swiss Alps that provides measurements representative of European background conditions, although it periodically receives polluted air from central Europe (57). Gosan is located in South Korea and receives diverse air masses including polluted air from China, Korea and Japan, as well as cleaner background air (58). Zeppelin (472 m above sea level) is an Arctic station on Svalbard that samples predominantly clean Arctic air, although episodically receives polluted air masses from Western Europe and Russia, particularly during winter and spring (59).

Figure 6a shows the annual mean HFO-1234ze(E) mixing ratios at the surface as simulated by GEOS-Chem. The simulated global average surface HFO-1234ze(E) mixing ratio is 0.10 ppt. Mixing ratios peak over major industrial regions in Eastern China (≈ 2.1 ppt), and the Middle East (≈ 1.5 ppt), followed by Europe and the US (≈ 1.0 ppt). Elevated HFO-1234ze(E) mixing ratios remain highly localised near emission sources. Figures 6b and c show simulated vertical cross sections of HFO-1234ze(E) mixing ratios. The majority of HFO-1234ze(E) reacts in the boundary layer, with limited transport into the mid-troposphere. There is some vertical transport, particularly northward towards the Arctic, driven by large-scale circulation patterns (60). The longitudinal cross section (Figure 6b) shows elevated HFO-1234ze(E) mixing ratios centred over key emissions regions, while the latitudinal cross section (Figure 6c) highlights the asymmetry between hemispheres, with elevated mixing ratios between 20 and 45°N where major emission sources are located and very low mixing ratios in the Southern Hemisphere.

Figure 7 compares the simulated mixing ratios to the 2020-2024 observations at the 8 AGAGE sites. The model captures broad spatial patterns between most sites. For example, the model reproduces the interhemispheric gradient, with higher mixing ratios at Northern Hemisphere sites compared to Southern Hemisphere sites, and seasonal patterns. However, there are notable discrepancies in absolute mixing ratios, with the model overestimating observations by a factor of 5 at Gosan and by a factor of 7 at Kennaook/Cape Grim. Averaged over all 8 sites, the model overestimates observed mixing ratios by roughly 60% (0.188 vs 0.114 ppt). However, the modelled mean is skewed by the high model bias at Gosan. Excluding this site reduces the model mean to 0.106 ppt. Further comparison statistics can be found in Table S2 in the supplement.

View Article Online
DOI: 10.1039/D6EA00034G

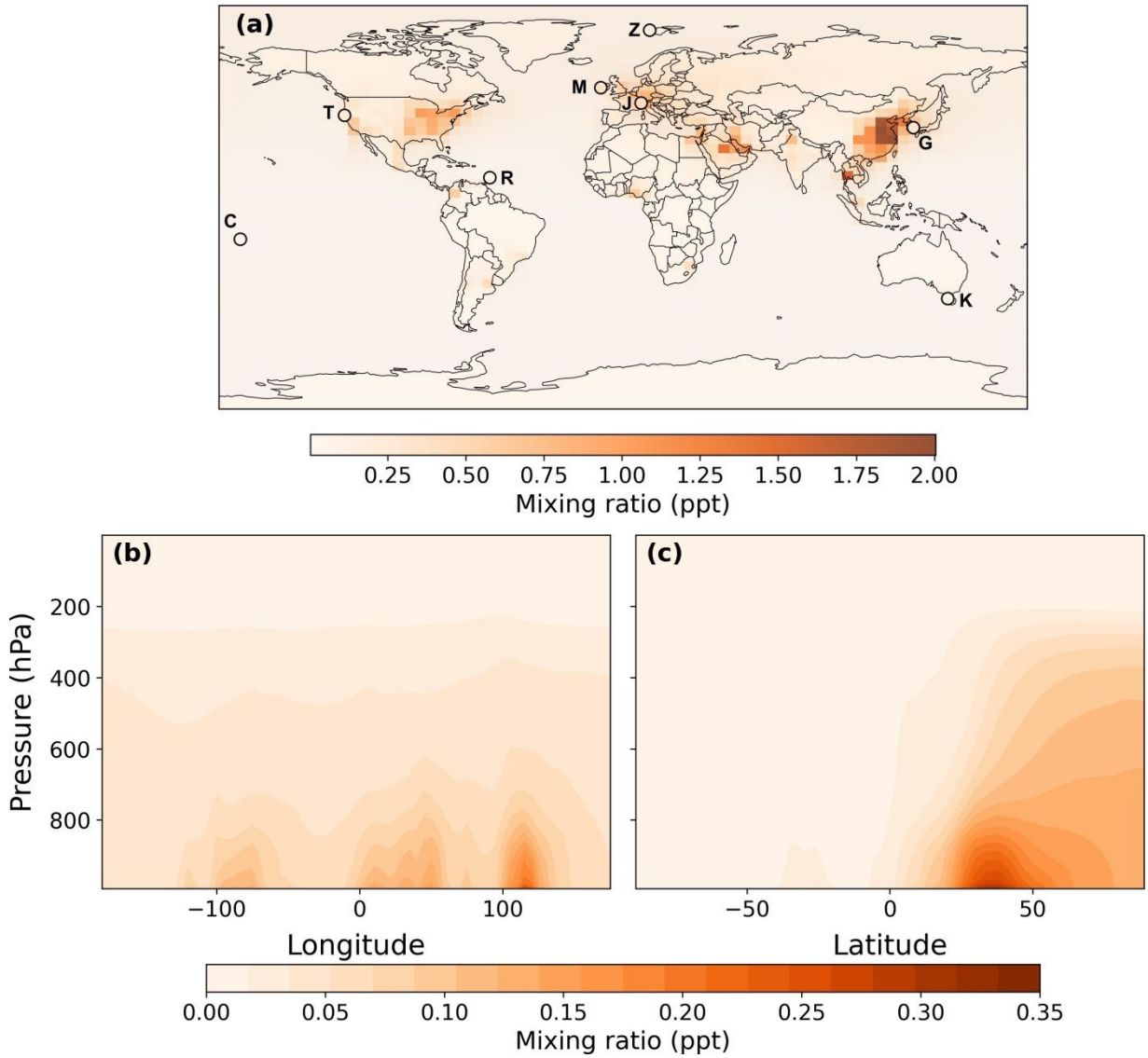

Figure 6: Annual average HFO-1234ze(E) mixing ratios simulated by GEOS-Chem a) at the surface, with 2022-2024 observed mixing ratios overlaid as filled circles, b) as a function of longitude and pressure (averaged over latitudes), and c) as a function of latitude and pressure (averaged over longitudes). Observation sites in a) are indicated by the first letter of the site name: Zeppelin (Z), Mace Head (M), Jungfraujoch (J), Trinidad Head (T), Gosan (G), Ragged Point (R), Cape Matatula (C), Kennaook/Cape Grim (K).

The biases in our simulation primarily reflect limitations in our emissions estimate, which uses 2018 HFC-134a emissions as a proxy in the absence of an existing bottom-up inventory for HFO-1234ze(E). Our results highlight the need for a dedicated inventory, with particular attention to the spatial distribution of emissions. At $4^\circ \times 5^\circ$ resolution, near-source concentration gradients and complex transport pathways are not

View Article Online
DOI: 10.1039/D6EA00034G

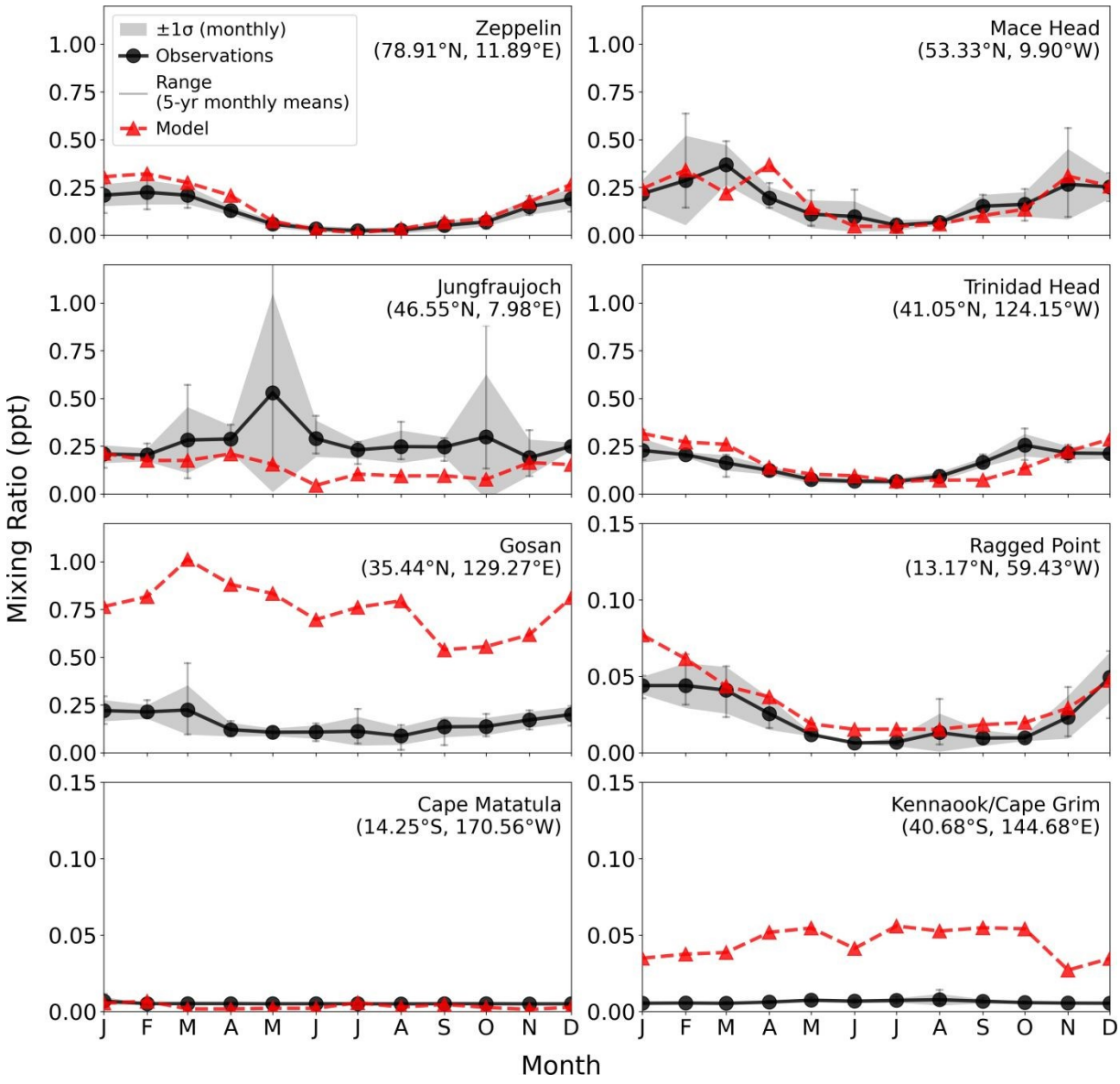

Figure 7: Seasonal cycles of HFO-1234ze(E) at eight Advanced Global Atmospheric Gases Experiment (AGAGE) network sites ordered by latitude from north to south. Observations (black circles, solid lines) show the mean seasonal cycle for 2020-2024, with shading indicating ±1 standard deviation of monthly means across the five years. Vertical bars indicate the full range of monthly mean values across those 5 years. Model results (red triangles, dashed lines) show the 2019 seasonal cycle. All data are monthly mean dry air mixing ratios expressed in units of parts per trillion (ppt). Observations are from Vollmer *et al.* (43).

well resolved, amplifying biases at sites such as Gosan that receive polluted air masses from multiple nearby source regions. Further, HFO-1234ze(E) adoption patterns likely differ across countries and application

View Article Online
DOI: 10.1039/D6EA00034G

sectors. For example, uptake rates may vary between China, Japan and South Korea in ways the HFC-134a distribution does not capture, leading to misallocation of regional emissions within East Asia. Gosan receives diverse air masses from all three countries and is particularly sensitive to this misallocation. By contrast, our European emissions total of 1.1 Ggyr^{-1} agrees well with the 0.96 Gg yr^{-1} reported by Vollmer et al. (43), providing confidence in the inventory where observational constraints are available and highlighting the need for improved constraints on East Asian emissions.

Remote background sites are less sensitive to the choice of emissions proxy because mixing ratios are controlled by total hemispheric emissions rather than their regional distribution, explaining the generally better model agreement at these sites. The exception is the high bias at Kennaook/Cape Grim, which likely reflects a mix of uncertainties in Southern Hemisphere mid-latitude emission totals and local oxidation chemistry. Overestimated interhemispheric exchange rates are unlikely to be drivers, as the interhemispheric exchange in GEOS-Chem has been validated in previous studies using long-lived tracers including SF_6 and CH_3CCl_3 (61), and HFO-1234ze(E) has a tropospheric lifetime of approximately 16 days, much shorter than the interhemispheric exchange time of approximately 1.4 years (61). In addition, there is no equivalent high bias at the more equatorward Cape Matatula site. Local chemistry, on the other hand, may play a role. Our simulations do not include Cl-initiated oxidation of HFO-1234ze(E) (6), as tropospheric Cl concentrations are roughly three orders of magnitude lower than OH concentrations (62) and therefore unlikely to be of major consequence at the global scale. However, at coastal sites such as Kennaook/Cape Grim, Cl concentrations can be elevated due to sea salt and halogen activation chemistry (8), and HFO-1234ze(E) loss to Cl oxidation could be higher locally. The regional impacts of this chemistry should be tested in future work; however, it is unlikely to have a significant impact on the overall global outcomes that are the focus of this work.

Despite lingering biases at individual sites, based on the model's ability to simulate the observed inter-hemispheric gradient, seasonal cycles, and order of magnitude of HFO-1234ze(E) mixing ratios, we consider our simulation sufficient for identifying broad global-scale impacts of HFO-1234ze(E) emissions. Two previous modelling studies of HFO-1234ze(E) degradation also provide useful benchmarks for our results. Wang *et al.* (8) used emissions of 12.6 Gg yr^{-1} over China in an alternative GEOS-Chem implementation and reported much higher surface mixing ratios of HFO-1234ze(E), with a global average of 0.55 ppt and 10.47 ppt over China. In comparison, our global emissions inventory assigns 3.9 Gg yr^{-1} to China (Figure 2). Despite our Chinese emissions being about three times lower than those from Wang *et al.*, our simulated HFO-1234ze(E) mixing ratios over China are approximately 20 times lower. With 15 Gg yr^{-1} of total global emissions distributed across all regions, our simulated global average mixing ratio ($\approx$ 0.1 ppt) is approximately five times lower than Wang *et al.*'s reported 0.55 ppt, based on 12.6 Gg yr^{-1} of emissions from China and none elsewhere. Our evaluation against AGAGE observations suggests our mixing ratios are more realistic than those simulated by Wang *et al.*, possibly due to differences in their model setup. Pérez-Peña *et al.* (5) used a box model to simulate the global boundary layer with 12.6 Gg yr^{-1} of emissions and calculated mixing

View Article Online
DOI: 10.1039/D6EA00034G

ratios of 0.08 ppt averaged over the global planetary boundary layer, consistent with our results.

3.3.2 Global distribution and budget of simulated CF_3CHO

Figure 8a shows the modelled mixing ratios of CF_3CHO at the surface. The highest CF_3CHO mixing ratios are found in regions with strong HFO-1234ze(E) emissions. The CF_3CHO atmospheric lifetime is much shorter than that of HFO-1234ze(E), and so CF_3CHO mixing ratios are significantly lower than for HFO-1234ze(E). The global annual average surface mixing ratio is 0.01 ppt. The highest CF_3CHO mixing ratios are in the Middle East (0.16 ppt), and Eastern China (0.11 ppt).

The HFO-1234ze(E) differences between our simulation and Wang *et al.* (8) discussed in the previous section propagated to the modelled CF_3CHO mixing ratios. Wang *et al.* reported an average global CF_3CHO surface mixing ratio of 0.18 ppt (8), compared to 0.01 ppt from our simulations. In addition to likely overestimating HFO-1234ze(E) in their model (as discussed above), Wang *et al.* did not include depositional losses for CF_3CHO, which we demonstrate below to be a significant sink. Our results are more consistent with those reported by Pérez-Peña *et al.*, who found an average global mixing ratio of 0.02 ppt (5).

Figures 8b and c show the vertical distribution of CF_3CHO mixing ratios. Although the highest HFO-1234ze(E) mixing ratios were found at the surface, the CF_3CHO mixing ratios peak around 900 hPa (≈2 km). This offset is primarily driven by the altitude dependence of the chemical lifetime of HFO-1234ze(E), shown in Figure S3 in the Supplementary Information. HFO-1234ze(E) is lost most rapidly at around 900 hPa, leading to enhanced production of CF_3CHO at this altitude. Surface removal processes such as dry deposition further suppress CF_3CHO mixing ratios near the ground.

Table 3 displays the global budget of atmospheric CF_3CHO. Sources and sinks of CF_3CHO are balanced over the year. The dominant sink is deposition, accounting for on average 51% of total CF_3CHO loss. Photolysis to CF_3 and HCO radicals (R4) represents the next largest CF_3CHO sink at 33%. This pathway does not produce HFC-23, which is formed from CF_3CHO exclusively via the concerted molecular elimination channel (R5). We tested the sensitivity of the CF_3CHO loss branching to uncertainty in the photolysis quantum yield using the AtChem2 box model. Varying the total photolysis quantum yield by ±20%, consistent with uncertainties reported by IUPAC, shifted the relative contributions of photolysis and OH to chemical loss by ±1.5%, indicating limited sensitivity to this parameter. Consistent with our box model results (Section 3.1), we find using GEOS-Chem that the net loss of CF_3CHO to reaction with HO_2 is small (0.14 Gg $year^{-1}$, 1.2%).

We added tracers to the chemical mechanism to quantify the extent to which CF_3CHO reacts with HO_2 (R6) before undergoing the reverse reaction (R6'). Although this reaction is the dominant initial pathway (with 88% of CF_3CHO first forming the $CF_3CHOHOO$ intermediate), the intermediate rapidly decomposes back to CF_3CHO + HO_2 under typical tropospheric conditions. As a result there is little net forward reaction. These results support our finding in Section 3.1 that the reaction between CF_3CHO and HO_2 is of

View Article Online
DOI: 10.1039/D6EA00034G

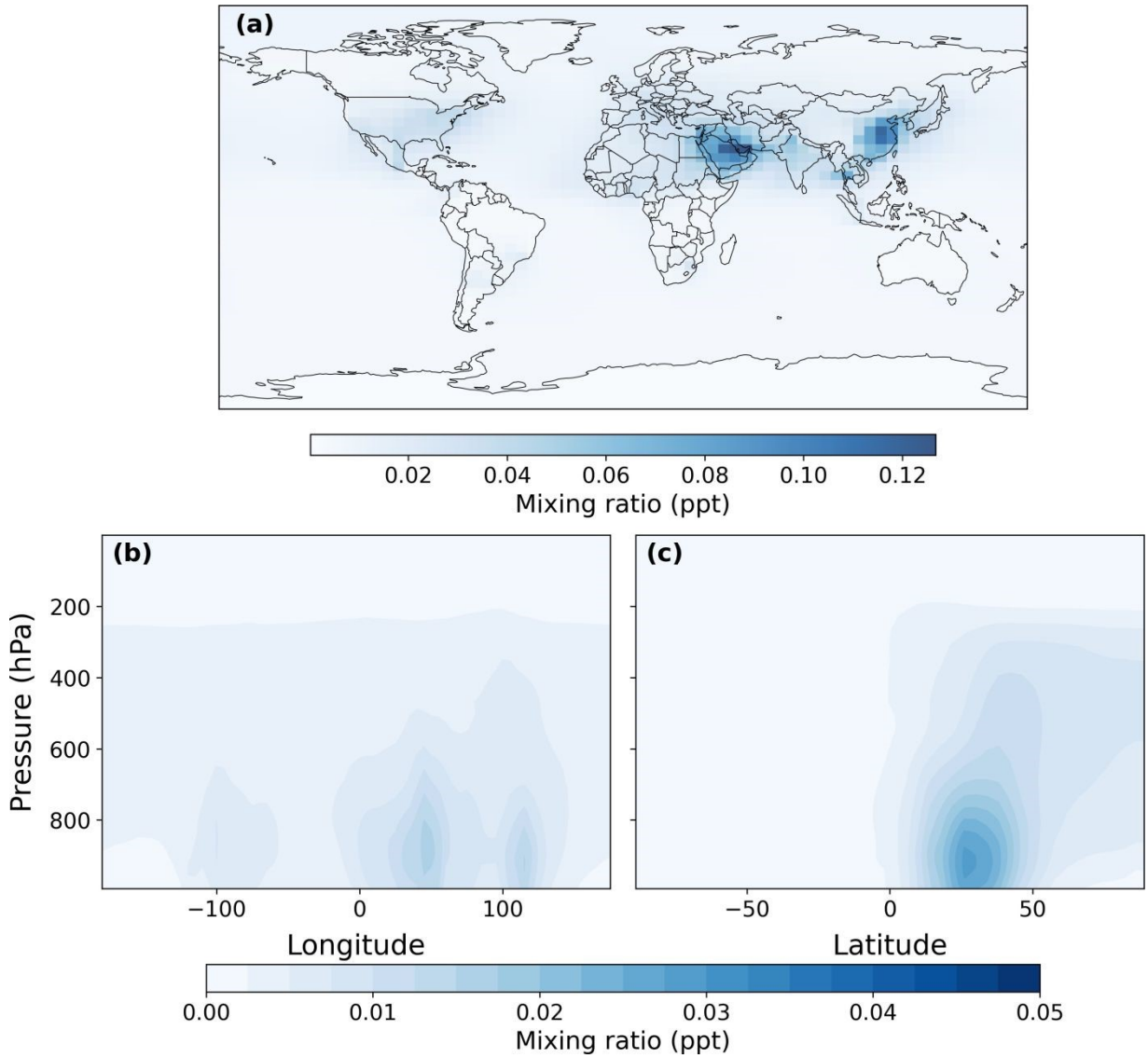

Figure 8: Annual average CF_3CHO mixing ratios simulated by GEOS-Chem a) at the surface, b) as a function of longitude and pressure (averaged over latitudes), and c) as a function of latitude and pressure (averaged over longitudes).

little atmospheric significance. Further comparison between the AtChem2-MCM and GEOS-Chem results can be found in the Supplementary Information (Section S1, Figure S4).

Figure 9 shows the relative contributions of the different loss processes to total CF_3CHO loss as a function of altitude. The loss mechanisms exhibit strong altitude dependence. At the surface, dry deposition accounts for almost 92%. Because dry deposition is confined to the surface layer, the sharp initial decrease in depositional loss with altitude is driven by the absence of this pathway above the surface. Photolysis processes

View Article Online
DOI: 10.1039/D6EA00034G

Table 3: Global sources and sinks of atmospheric CF_3CHO from HFO-1234ze(E) oxidation.

Sources/Sinks	Absolute (Gg yr^{-1})	Relative (%)
HFO-1234ze(E) oxidation	12.5	100
Total Sources	**12.5**	**100**
Photolysis (CF_3 + HCO)	4.1	32.5
Wet Deposition	3.9	31.0
Dry Deposition	2.5	19.8
OH Oxidation	1.9	15.4
Reaction with HO_2	0.1	1.2
Photolysis (HFC-23 + CO)	0.01	0.1
Total Sinks	**12.5**	**100**

become increasingly important in the upper atmosphere, where UV radiation is more intense, quantum yields are higher (lower pressure) and water vapour drops off. The reaction with HO_2, shown in purple, exhibits a notable pressure dependence. At the surface, this process contributes less than 0.1% to total CF_3CHO loss, consistent with our AtChem2 box model (Section 3.1, Figure 3b). However, the contribution increases with altitude, reaching 80% in the upper troposphere due to the pressure-dependent forward rate coefficient (R6). Despite this altitude dependence, the global column-integrated contribution remains small (0.7%, Table 3, Figure 9b) because the $CF_3CH(OH)OO$ intermediate formed in the forward reaction rapidly decomposes back to CF_3CHO + HO_2 under typical tropospheric conditions. The altitude profile in Figure 9 reveals that while the forward reaction becomes more favourable at lower pressures, the net atmospheric significance of this pathway remains limited even in the upper troposphere, confirming our box model conclusions that this recently identified reaction (5) does not substantially alter the atmospheric fate of CF_3CHO. The contribution of the photolysis channel leading to HFC-23 production (shown in dark orange) also increases as pressure decreases, rising from less than 0.01% at the surface to a maximum of 0.4% at 300 hPa.

The CF_3CHO lifetime as simulated by GEOS-Chem is shown in Table 4 and Figure S3 in the Supplementary Information for both January and July. We find a tropospheric lifetime for CF_3CHO of 2.1 days, with individual contributions of 3.7-4.6 days against deposition, 5.3-8.5 days against photolysis, and 9.2-21.4 days against OH oxidation. The lifetimes vary seasonally, with shorter lifetimes in boreal summer for all processes due to faster deposition, OH reaction and photolysis. Our results are in close agreement with the overall 2.2 day tropospheric lifetime estimated in the SAP report (40) and substantially lower than the 13 ± 4 days lifetime at 5 km altitude reported by Sulbaek Andersen *et al.* (41), who did not include depositional losses. For individual processes, our photolysis lifetime is close to the values reported by Chiappero *et al.* (28) and

View Article Online
DOI: 10.1039/D6EA00034G

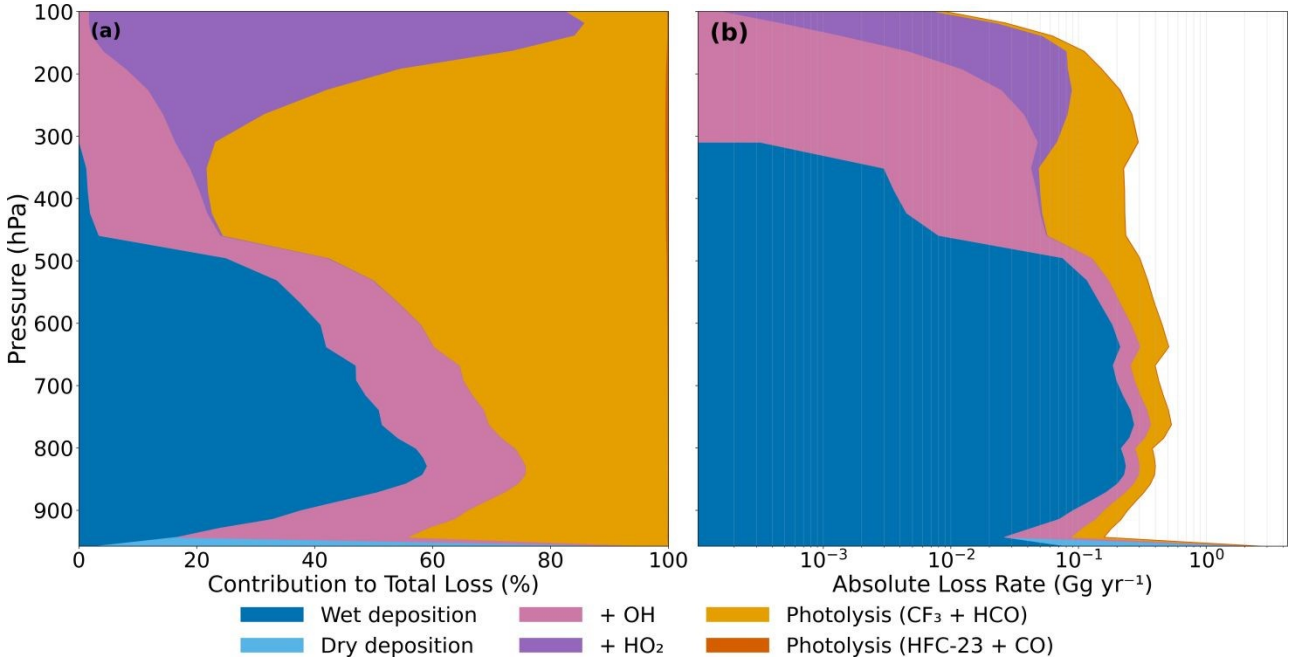

Figure 9: Altitude dependence of CF_3CHO loss pathways from HFO-1234ze(E) degradation as simulated by GEOS-Chem. (a) Fractional contribution to annual mean total loss at each pressure level. (b) Absolute annual loss rates at each pressure level. Note that dry deposition is a surface-only process.

Nielsen *et al.* (24), who estimated 3-6 days and 7 days, respectively. Our deposition lifetime is consistent with the estimates of 4-8 days by Nielsen *et al.* (24) (wet scavenging only) and 5.5 days by Pérez-Peña *et al.* (25) (wet and dry deposition), both assuming K_H^* of CF_3CHO of order 10^4 M atm^{-1} (vs. 10^5 M atm^{-1} here). Our OH oxidation lifetimes exhibit significant seasonal variability, ranging from 9.2 days to 21.4 days, compared to the 20 day lifetime reported by Nielsen *et al.* (24).

3.3.3 HFC-23 production

Figure 10a displays the average annual production rates of HFC-23 from HFO-1234ze(E) ozonolysis (R2) and CF_3CHO photolysis (R5) in surface air. For HFC-23, we show production rates rather than mixing ratios because the long HFC-23 lifetime leads to minimal spatial variability in mixing ratios. Production rates more clearly indicate where and how photochemical pathways are influencing the HFC-23 distribution. As expected, the spatial distribution of HFC-23 production rates in surface air resembles that of the HFO-1234ze(E) and CF_3CHO mixing ratios (Figures 6, 8). Figures 10b and 10c display vertical cross sections of the HFC-23 production rates. While CF_3CHO and HFO-1234ze(E) mixing ratios decrease with altitude, HFC-23 production peaks well above the surface. The photolytic reaction that generates HFC-23 (R5) has an inverse pressure dependence, enhancing HFC-23 production at higher altitudes. This results in HFC-23 chemical production rates that persist with relatively little decrease up to around 600 hPa, well above the

View Article Online
DOI: 10.1039/D6EA00034G

Table 4: CF_3CHO lifetimes in the troposphere with respect to different loss processes using K^*_H = 10^5 M atm^{-1}.

	Lifetime (days)				
Loss Process	**Annual**	**DJF**	**MAM**	**JJA**	**SON**
Deposition (dry + wet)	4.2	4.3	4.6	3.7	4.2
Photolysis (CF_3 + HCO)	6.6	8.5	6.0	5.3	7.1
Oxidation by OH	13.9	21.4	14.1	9.2	14.3
Overall Lifetime	**2.1**	**2.5**	**2.2**	**1.7**	**2.2**

peak of the CF_3CHO mixing ratios (Figure 8b).

Using the simulated production rates, we calculate total HFC-23 production to be approximately 11 Mg yr^{-1} during our one-year global simulation. This corresponds to a growth rate of less than 0.001 ppt yr^{-1}, three orders of magnitude smaller than the observed annual increase of 1 ppt yr^{-1} (63). Therefore, our simulations indicate that HFO-1234ze(E) emission makes a negligible contribution to current HFC-23 growth. We note that our choice of K^*_H is at the upper end of the plausible range, and a lower K^*_H would reduce CF_3CHO loss to deposition, potentially increasing loss to photolysis and associated HFC-23 production. In addition, the substantial growth in HFO emissions projected for some parts of the world (8, 64) would increase the additional HFC-23 source from HFO-1234ze(E). Regardless of these uncertainties, we expect HFC-23 production from HFO-1234ze(E) to remain small relative to the present-day HFC-23 growth rate.

In our simulations, 99.6% of HFO-1234ze(E) reacts with OH to form CF_3CHO, with the remainder undergoing ozonolysis. Since ozonolysis forms HFC-23 from HFO-1234ze(E) rather than via CF_3CHO, we treat these pathways differently. We calculate an overall atmospheric molar yield of HFC-23 from CF_3CHO of 9.0×10^{-4} mol mol^{-1}. Combining our calculated HFC-23 yield from CF_3CHO with the published GWP_{100} of HFC-23 (14,600 (14)), we calculate an indirect GWP_{100} of 8.2 for HFO-1234ze(E) from the CF_3CHO photolysis pathway. The uncertainty in the indirect GWP_{100} from the CF_3CHO photolysis pathway is dominated by the uncertainty in φ_5. Van Hoomissen *et al.* report $\varphi_5 = (3.02 \pm 0.70) \times 10^{-4}$ at 308 nm and 650 Torr, corresponding to a relative uncertainty of approximately 23% (19). Since HFC-23 production scales linearly with φ_5, this propagates directly to the indirect GWP_{100} from photolysis, giving 8.2 ± 1.9. Additional uncertainty arises from K^*_H, which we have partially characterised through sensitivity tests in Section 3.2. Reducing K^*_H from 10^5 to 10^3 M atm^{-1} decreases CF_3CHO deposition by 30%, resulting in proportional increases to other loss process and thereby to the indirect GWP_{100} from photolysis. Increasing K^*_H from 10^5 M atm^{-1} has no impact on the fate of CF_3CHO, so there is no equivalent decrease in the indirect GWP_{100} from photolysis. Incorporating both of these uncertainties, our calculated indirect GWP_{100} from photolysis is $8.2^{+3.1}_{-1.9}$.

View Article Online
DOI: 10.1039/D6EA00034G

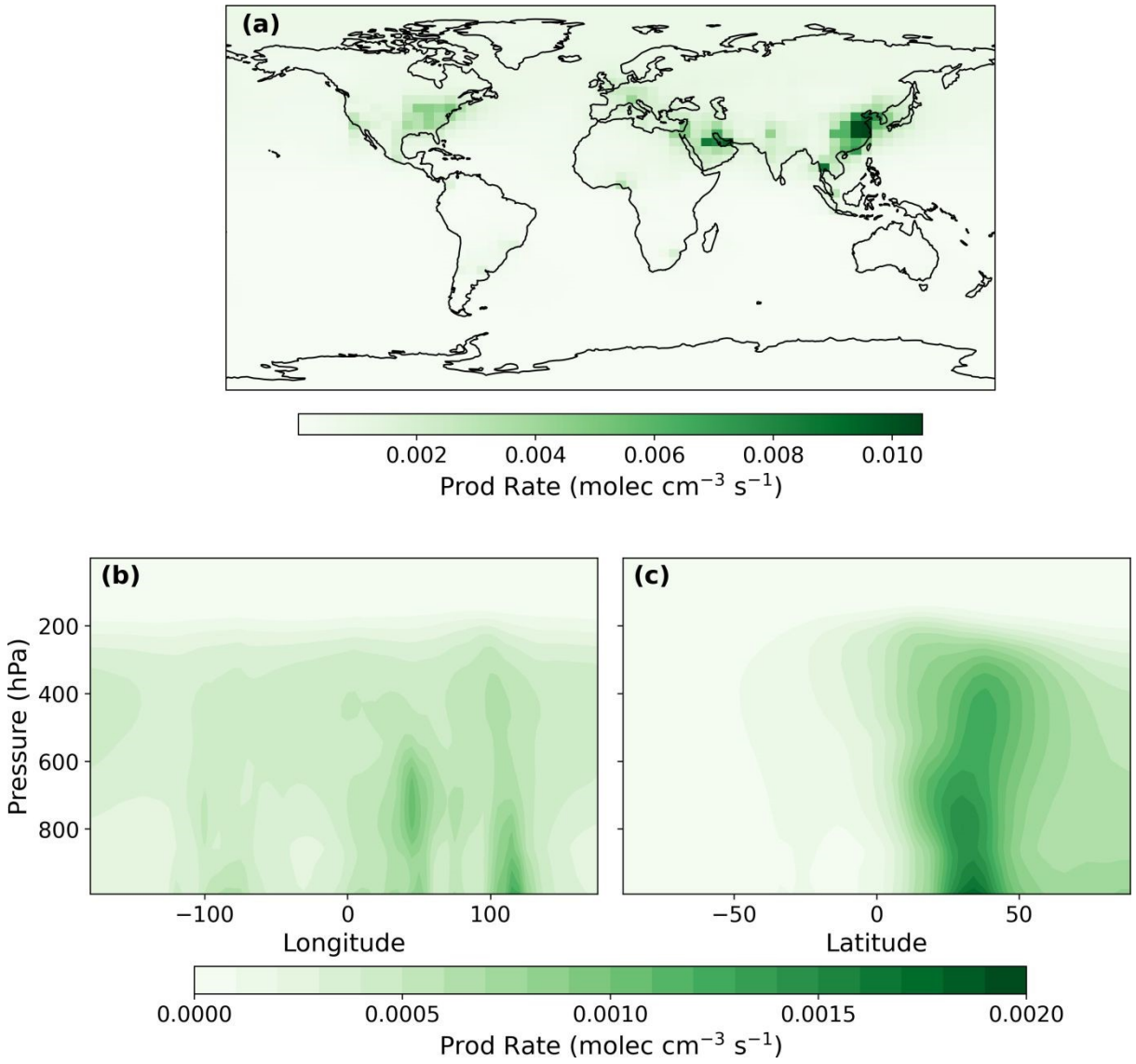

Figure 10: Annual average HFC-23 production rates simulated by GEOS-Chem a) at the surface b) as a function of longitude and pressure (averaged over latitudes) and c) as a function of latitude and pressure (averaged over longitudes).

Recent experimental work provides benchmarks for the molar yield of HFC-23 from CF_3CHO. Most recently, Van Hoomissen *et al.* (19) reported a molar product yield for HFC-23 formation from CF_3CHO of $(1.71 \pm 0.70) \times 10^{-3}$ mol mol^{-1} at 308 nm, 650 Torr. This is in close agreement with Thomson *et al.* (18), who reported a molar yield of HFC-23 from CF_3CHO of $(1.17 \pm 0.27) \times 10^{-3}$ mol mol^{-1} at 308 nm, 1 bar N_2. Thomson *et al.* also estimated an atmospheric molar yield of HFC-23 from HFO-1234ze(E) of 6.4×10^{-4} mol mol^{-1}, assuming 41% depositional loss of CF_3CHO (vs. 50% here), from which they estimated an indirect

View Article Online
DOI: 10.1039/D6EA00034G

GWP_{100} of around 6. Our results are consistent with these estimates.

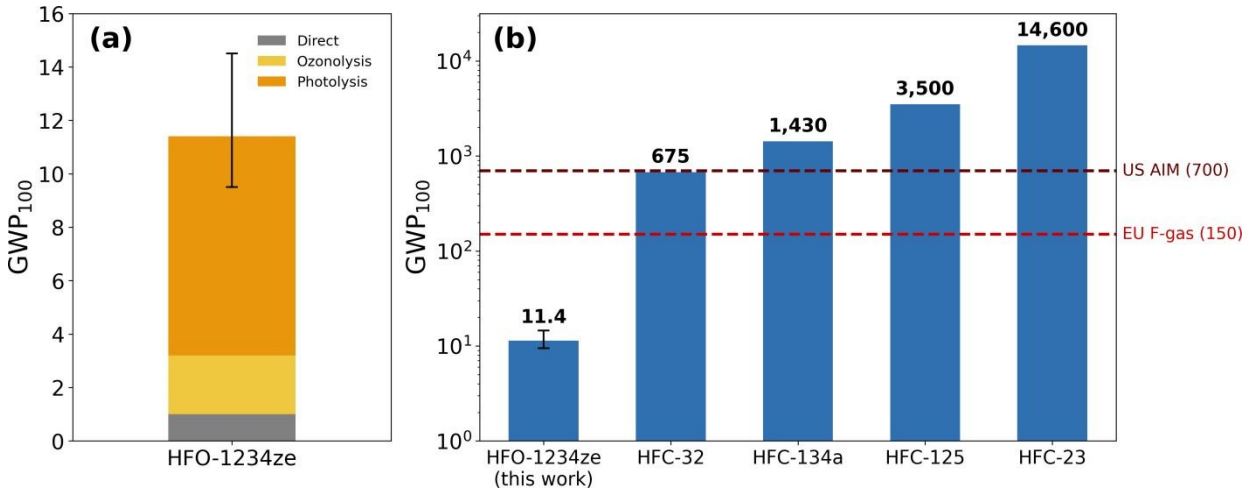

Figure 11: (a) Total GWP_{100} of HFO-1234ze(E), separated into contributions from direct radiative forcing (grey) and indirect effects from HFC-23 formation via HFO-1234ze(E) ozonolysis (yellow) and HFC-23 formation via CF_3CHO photolysis (orange). Error bars indicate the combined uncertainty from the CF_3CHO photolysis quantum yield (±23%) and Henry's Law constant sensitivity K_H^* = $10^3 - 10^5$ M atm^{-1}. (b) Comparison of the HFO-1234ze(E) GWP_{100} calculated in this work with common HFCs on a logarithmic scale. Dashed lines indicate regulatory thresholds under EU F-gas regulations (150) and the US AIM Act (700) (65, 66).

Our simulation also includes HFC-23 production from HFO-1234ze(E) ozonolysis, yielding an indirect GWP_{100} of 2.2±0.3. We find ozonolysis accounts for 0.36% of total HFO-1234ze(E) loss - substantially lower than the 2.96% initially reported by McGillen *et al.* (7) but consistent with their updated model estimates reported in Garavagno *et al.* (20). Our results are also consistent with theoretical expectations: assuming average mixing ratios of OH (1×10^6 molecules cm^{-3}) and O_3 (7.5×10^{11} molecules cm^{-3}) (67, 68) with rate coefficients at 298 K, we calculate an ozonolysis contribution of ~0.4%, consistent with our 3-D model results. The k_{O_3}/k_{OH} ratio at 298 K (3.46×10^{-9}) falls below the 10^{-8} threshold where ozonolysis typically becomes significant (69). While k_{OH} is temperature-dependent, our 3-D simulations account for this variability across all atmospheric conditions and confirm that ozonolysis remains a minor contributor to both HFO-1234ze(E) loss and HFC-23 formation globally.

The combined indirect GWP_{100} of HFO-1234ze(E) from HFC-23 formed via ozonolysis (GWP_{100}=2.2±0.3) and via photolysis of CF_3CHO ($GWP_{100}=8.2^{+3.1}_{-1.9}$) is around $GWP_{100}=10.4^{+3.1}_{-1.9}$. There is also a direct radiative forcing contribution from HFO-1234ze(E) with a GWP_{100} of approximately 1 (3, 70). These contributions are shown together in the bar chart in Figure 11a. Taken together, our results imply a total GWP_{100} (indirect + direct) for HFO-1234ze(E) of $GWP_{100}=11.4^{+3.1}_{-1.9}$Note that the uncertainty reported here does not include

View Article Online
DOI: 10.1039/D6EA00034G

uncertainties in emissions or other parameters of the global transport model.

Although an order of magnitude larger than the currently reported total GWP_{100}, Figure 11b shows that the updated HFO-1234ze(E) GWP_{100} determined in this work is far below the threshold of concern in current regulatory frameworks, even under the most conservative combination of assumptions (lower bound K^*_H and upper bound φ_5). Under the European Union F-gas regulation, the use of F-gases is prohibited in commercial refrigeration systems if their total GWP_{100} exceeds 150, and in industrial refrigeration if it exceeds 2500 (65). Similar thresholds are being adopted by the US legislation under the American Innovation and Manufacturing (AIM) Act, which will restrict refrigerants to GWP_{100} values below 700, 300, or 150, depending on the use (66). Against these benchmarks, the total GWP_{100} we calculate for HFO-1234ze(E) is of no regulatory significance. This value also remains far below the GWP_{100} of the HFCs that HFO-1234ze(E) is designed to replace, including HFC-134a (GWP_{100}=1430), HFC-32 (GWP_{100}=675), and HFC-125 (GWP_{100}=3500), as shown in Figure 11b. Even accounting for the uncertainties in the indirect contributions quantified in this work, HFO-1234ze(E) offers a climate benefit of roughly two orders of magnitude compared to these legacy refrigerants.

4 Conclusions

Despite its increasing use as a replacement for ozone-destroying and climate-warming CFCs, HCFCs and HFCs, the true climate impact of HFO-1234ze(E) is not well characterised. In this work, we modelled the degradation of HFO-1234ze(E) using the GEOS-Chem 3-D chemical transport model to quantify the fates of HFO-1234ze(E) and its primary oxidation product CF_3CHO, the resulting production of the potent greenhouse gas HFC-23, and the total GWP_{100} of HFO-1234ze(E) accounting for indirect effects. We modified GEOS-Chem to add the relevant chemistry, including newly determined reaction rate constants and photolysis quantum yields. We also used the AtChem2 box model with MCM v3.3.1 to test specific aspects of the chemistry before implementation in GEOS-Chem. We developed two emissions scenarios: a China-only emission scenario assuming complete HCFC-141b replacement (12.6 Gg yr^{-1}) following previous work (5, 8) that we used for Henry's Law sensitivity studies, and a new global emission scenario with 15 Gg yr^{-1} distributed using HFC-134a emissions patterns and scaled to match observational constraints that we used for all other results.

We tested the recently proposed $CF_3CHO + HO_2$ reaction (13) using the AtChem2 box model incorporating the MCMv3.3 and found the net reaction contributes less than 0.1% to CF_3CHO removal at the surface because the product of the forward reaction rapidly decomposes back to its reactants. We then assessed the sensitivity of CF_3CHO loss to the effective Henry's Law Constant, K^*_H, using GEOS-Chem. In the absence of experimental measurements of K^*_H(CF_3CHO), we tested a range of values from 10 - 10^6 M atm^{-1}. We found that wet deposition saturates for K^*_H above 10^4 M atm^{-1}, with the choice of K^*_H fundamental to the atmospheric fate of CF_3CHO. Our results show that at high K^*_H deposition accounts for up to 60% of total

View Article Online
DOI: 10.1039/D6EA00034G

CF_3CHO loss, but this varies considerably with K^*_H. Without measurements of K^*_H (CF_3CHO), significant uncertainty remains. Future experimental determination of K^*_H is required to reduce these uncertainties.

Using an upper bound of K^*_H = 10^5 M atm^{-1} and global HFO-1234ze(E) emissions of 15 Gg yr^{-1}, we found good agreement between GEOS-Chem simulated HFO-1234ze(E) and observations at 8 AGAGE sites representing diverse global environments. The model reasonably captures both the magnitude and seasonal variability of HFO-1234ze(E) mixing ratios across Northern and Southern Hemisphere sites. We find that 99.6% of HFO-1234ze(E) is removed by reaction with OH, with the remaining 0.4% undergoing ozonolysis. Our simulations reveal that the atmospheric fate of CF_3CHO is dominated by deposition (51%) and photolysis (33%), with reaction with OH playing a more minor role (15%). The choice of Henry's Law constant affects the balance between these loss pathways: at K^*_H = 10^5 M atm^{-1}, deposition becomes a major sink, reducing the amount of CF_3CHO available for photolysis. This has direct implications for HFC-23 formation, as photolysis is the only pathway that produces HFC-23 from CF_3CHO. We calculate a global tropospheric CF_3CHO lifetime of 2.1 days, consistent with previous estimates (40). The overall atmospheric fate of HFO-1234ze(E) and CF_3CHO is summarised in Figure 12.

From our simulations, we estimate total HFC-23 production of approximately 11 Mg yr^{-1}, which corresponds to an HFC-23 growth rate of less than 0.001 ppt yr^{-1}. This is negligible compared to the current observed annual increase of 1 ppt yr^{-1} (63). Our findings result in an indirect GWP_{100} of $10.4^{+3.1}_{-1.9}$ for HFO-1234ze(E), of which $8.2^{+3.1}_{-1.9}$ is due to photolysis of the CF_3CHO intermediate and the 2.2±0.3 from HFO-1234ze(E) ozonolysis. The indirect GWP_{100} from CF_3CHO photolysis is similar to the recently reported value of 6 estimated from experimental measurements of the quantum yield (18). Combined with the direct GWP_{100} of approximately 1 (3, 70), the total GWP_{100} for HFO-1234ze(E) is $11.4^{+3.1}_{-1.9}$ well below the current legislative thresholds everywhere in the world (65, 66), and substantially lower than the GWP_{100} values of the HFCs that HFO-1234ze(E) is replacing (e.g., 1430 for HFC-134a). This total GWP_{100} estimate represents a lower bound due to our use of the upper bound K^*_H = 10^5 M atm^{-1}, which maximises deposition and therefore minimises HFC-23 formation via photolysis of CF_3CHO. If the true K^*_H is lower, e.g. 10^3 M atm^{-1}, our sensitivity tests (Section 3.2) indicate that deposition would decrease by 30%, increasing the indirect GWP_{100} contribution proportionally. However, even under this scenario, the total GWP_{100} remains well below regulatory thresholds (66) (65), and represents a substantial improvement over the HFCs it is replacing. Experimental measurement of K^*_H would refine this estimate but would not alter the fundamental conclusions.

The dominant role of deposition as a CF_3CHO sink has implications for the formation of trifluoroacetic acid (TFA). TFA is resistant to atmospheric degradation and accumulates in the environment, particularly in water bodies (71, 72). We find from our simulation using K^*_H =10^5 M atm^{-1} (an upper bound) that up to 31% of CF_3CHO may undergo wet deposition. When CF_3CHO comes into contact with water, it hydrates to form the stable gem-diol $CF_3CH(OH)_2$ (24), which is then almost completely oxidised to TFA (73). Using this

View Article Online
DOI: 10.1039/D6EA00034G

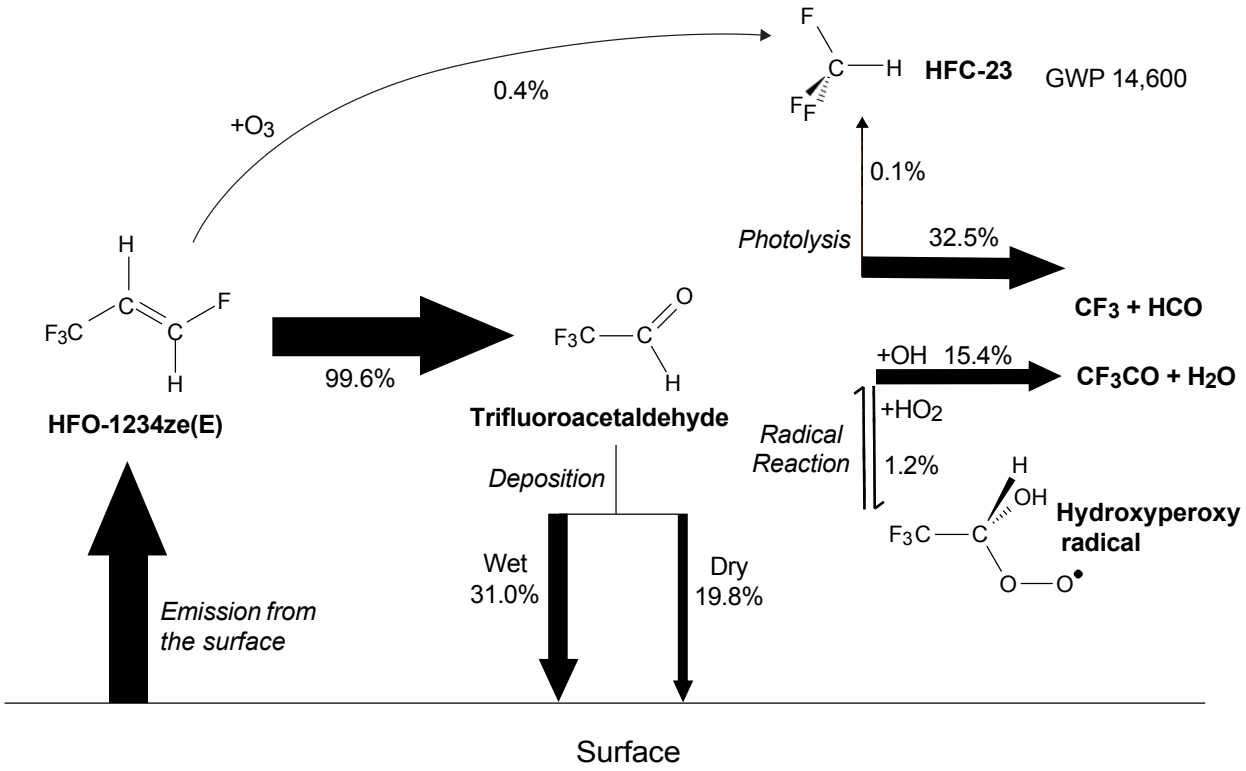

Figure 12: Summary of the atmospheric fate of HFO-1234ze(E) and its primary oxidation product CF_3CHO as simulated by GEOS-Chem using $K_H^* = 10^5$ M atm^{-1}. Percentages indicate the fraction of total removal attributed to each pathway. Note that 0.36% of HFO-1234ze(E) reacts with ozone, and this process produces HFC-23 with a yield of 7.9% (20). CF_3CHO loss is dominated by deposition (51%), followed by photolysis (33%) and reaction with OH (15%). The $CF_3CHO + HO_2$ reaction accounts for a net 1.2% of CF_3CHO removal.

upper bound, and assuming complete hydrolysis of all-wet deposited CF_3CHO to TFA from HFO-1234ze(E) degradation yields a maximum potential formation of 4.5 Gg yr^{-1}. This represents the maximum theoretical TFA formation from this source. Our sensitivity tests (Section 3.2) show that reducing K_H^* from 10^5 to 10^3 M atm^{-1} decreases the wet deposition fraction from ~31% to ~22%, corresponding to a TFA formation range of approximately 2.8-4.5 Gg yr^{-1}. For context, 2022 global TFA deposition from HCFC and HFC sources was estimated as 21.8 Gg yr^{-1} (74). These results suggest that wet deposition of CF_3CHO formed via HFO-1234ze(E) oxidation may be a previously unrecognised source of TFA accumulation, particularly in regions close to emission sources.

Author Contributions

BK conducted the GEOS-Chem and AtChem2 simulations, analysed the data, and prepared the manuscript. JAF, CSH and SHK supervised the research and contributed to manuscript preparation. MKV and PBK

View Article Online
DOI: 10.1039/D6EA00034G

provided observational data from AGAGE measurements, assisted with model-observation comparisons and data analysis, and contributed to manuscript preparation. All authors reviewed and approved the final manuscript.

Conflicts of Interest

There are no conflicts to declare.

Acknowledgments

The authors thank Paolo Sebastianelli and Stephen MacFarlane for their assistance with GEOS-Chem model configuration and development. This research was supported by the Australian Research Council grants DP220102466 and DP220100891). The work was undertaken with the assistance of resources provided at the NCI National Facility systems at the Australian National University through the National Computational Merit Allocation Scheme supported by the Australian Government (project q90).

Data Availability

Observational data for HFO-1234ze(E) were obtained from the Advanced Global Atmospheric Gases Experiment (AGAGE) network. AGAGE data are available from https://doi.org/10.5194/egusphere-2025-4824. GEOS-Chem model configuration files and emissions inventories are available at https://github.com/bethkillen. GEOS-Chem (https://geos-chem.readthedocs.io/en/stable/) and AtChem2 (https://github.com/AtChem/AtChem2) are open-source software. The full model output is available on request.

View Article Online
DOI: 10.1039/D6EA00034G

References

[1] United Nations Environment Programme Montreal Protocol on Substances that Deplete the Ozone Layer. 1987; https://ozone.unep.org/treaties/montreal-protocol, 26 I.L.M. 1550.

[2] United Nations Environment Programme Kigali Amendment to the Montreal Protocol on Substances that Deplete the Ozone Layer. 2016; https://ozone.unep.org/treaties/montreal-protocol/amendments/kigali-amendment, C.N.872.2016.TREATIES-XXVII.2.f.

[3] Inc., H. I. Solstice® ze Refrigerant (HFO-1234ze (E)): The Environmental Alternative to Traditional Refrigerants Ultra-low GWP Hydrofluoroolefins (HFO); Technical Data Sheet. 2018.

[4] Khan, M. A. H. et al. Global modeling of trifluoroacetic acid surface concentration and deposition from the gas-phase oxidation of a wide range of precursor hydrofluoroolefins. *Environmental Science: Atmospheres* **2026**, *6*, 195–212.

[5] Pérez-Peña, M. P.; Fisher, J. A.; Hansen, C.; Kable, S. H. Assessing the atmospheric fate of trifluoroacetaldehyde (CF_3CHO) and its potential as a new source of fluoroform (HFC-23) using the AtChem2 box model. *Environ. Sci.: Atmos.* **2023**, *3*, 1767–1777.

[6] Javadi, M. S.; Søndergaard, R.; Nielsen, O. J.; Hurley, M. D.; Wallington, T. J. Atmospheric chemistry of trans-CF_3CH=CHF: products and mechanisms of hydroxyl radical and chlorine atom initiated oxidation. *Atmospheric Chemistry and Physics* **2008**, *8*, 3141–3147.

[7] McGillen, M. R.; Fried, Z. T. P.; Khan, A. H.; Kuwata, K. T.; Martin, C. M.; O'Doherty, S.; Pecere, F.; Shallcross, D. E.; Stanley, K. M.; Zhang, K. Ozonolysis can produce long-lived greenhouse gases from commercial refrigerants. *Proceedings of the National Academy of Sciences* **2023**, *120*, e2312714120.

[8] Wang, Y.; Wang, Z.; Sun, M.; Guo, J.; Zhang, J. Emissions, degradation and impact of HFO-1234ze from China PU foam industry. *Science of The Total Environment* **2021**, *780*, 146631.

[9] Wallington, T. J.; Hurley, M. D.; Schneider, W. F. Kinetic Study of the Reaction $CF_3O + O_3 \rightarrow CF_3O_2 + O_2$. *Chemical Physics Letters* **1993**, *213*, 442–448.

[10] Francisco, J. S. On the Mechanism of the Gas-Phase Hydrolysis of Carbonyl Fluoride. *Journal of the American Chemical Society* **1993**, *115*, 6045–6046.

[11] Zachariah, M. R.; Westmoreland, P. R.; Burgess, D. R. A Study of the Gas-Phase Reaction of Carbonyl Fluoride with Water. *The Journal of Physical Chemistry* **1995**, *99*, 11801–11808.

[12] Wallington, T. J.; Hurley, M. D.; Nielsen, O. J.; Sehested, J. Atmospheric Chemistry of CF_3COx Radicals: Fate of CF_3CO Radicals, the UV Absorption Spectrum of $CF_3C(O)O_2$ Radicals, and Kinetics of

View Article Online
DOI: 10.1039/D6EA00034G

the Reaction $CF_3C(O)O_2 + NO \rightarrow CF_3C(O)O + NO_2$. *The Journal of Physical Chemistry* **1994**, *98*, 5686–5694.

[13] Long, B.; Xia, Y.; Truhlar, D. G. Quantitative Kinetics of HO2 Reactions with Aldehydes in the Atmosphere: High-Order Dynamic Correlation, Anharmonicity, and Falloff Effects Are All Important. *Journal of the American Chemical Society* **2022**, *144*, 19910–19920, PMID: 36264240.

[14] Masson-Delmotte, V. et al. *Climate Change 2021: The Physical Science Basis*; Cambridge University Press: Cambridge, United Kingdom and New York, NY, USA, 2021.

[15] Dodd, R. E.; Smith, J. W. 282. The photolysis of trifluoroacetaldehyde. *J. Chem. Soc.* **1957**, 1465–1473.

[16] Pearce, C.; Whytock, D. A. The photolysis of trifluoroacetaldehyde at 313 nm. *J. Chem. Soc. D* **1971**, 1464–1466.

[17] Sulbaek Andersen, M. P.; Nielsen, O. J. Tropospheric photolysis of CF_3CHO. *Atmospheric Environment* **2022**, *272*, 118935.

[18] Thomson, J. D.; Campbell, J. S.; Edwards, E. B.; Medcraft, C.; Nauta, K.; Pérez-Peña, M. P.; Fisher, J. A.; Osborn, D. L.; Kable, S. H.; Hansen, C. S. Fluoroform (CHF_3) Production from CF_3CHO Photolysis and Implications for the Decomposition of Hydrofluoroolefins and Hydrochlorofluoroolefins in the Atmosphere. *Journal of the American Chemical Society* **2025**, *147*, 33–38, PMID: 39714911.

[19] Van Hoomissen, D.; Chattopadhyay, A.; Montzka, S. A.; Burkholder, J. B. CHF3 (HFC-23) and CF3CHO Quantum Yields in the Pulsed Laser Photolysis of CF_3CHO at 248, 266, 281, and 308 nm. *ACS Earth and Space Chemistry* **2025**, *9*, 589–602.

[20] Garavagno, M. d. l. A.; Wenger, A.; Holland, R. E. T.; Fena, B. R.; Goldstein, S. D.; Hicks, D. E.; Liu, F.; Madell, J. B.; Solomon, S. J.; Kuwata, K. T.; McGillen, M. R.; Khan, M. A. H.; Shallcross, D. E.; Stanley, K. M.; Orr-Ewing, A. J. Atmospheric Oxidation of Hydrofluoroolefins and Hydrochlorofluoroolefins by Ozone Produces HFC-23, PFC-14, and CFC-13. *Environmental Science & Technology* **2025**, *0*, null, PMID: 41317145.

[21] Harp International Ltd. *Safety Data Sheet: R1234ze (trans-1,3,3,3-tetrafluoropropene)*; Safety Data Sheet, 2020.

[22] Tewari, S. G.; Vijayaraghavan, K.; Zhao, K.; David, L. M.; Tuite, K.; Kristanovich, F.; Zhuang, Y.; Yang, B.; Hurtado, C.; Papanastasiou, D. K.; Giffen, P.; Kimko, H.; Gibbs, M.; Platz, S. Atmospheric and watershed modelling of HFO-1234ze(E) emissions from prospective pressurized metered-dose inhalers usage. *EGUsphere* **2025**, *2025*, 1–21.

View Article Online
DOI: 10.1039/D6EA00034G

[23] Sulbaek Andersen, M. P.; Schmidt, J. A.; Volkova, A.; Wuebbles, D. J. A three-dimensional model of the atmospheric chemistry of E and Z-CF_3CH – CHCl (HCFO-1233(zd) (E/Z)). *Atmospheric Environment* **2018**, *179*, 250–259.

[24] Nielsen, O. J.; Sulbaek Andersen, M. P.; Franklin, J. Comment on "Assessing the atmospheric fate of trifluoroacetaldehyde (CF_3CHO) and its potential as a new source of fluoroform (HFC-23) using the AtChem2 box model" by Pérez-Peña et al., Environ. Sci.: Atmos., 2023, 3, 1767–1777, DOI: 10.1039/D3EA00120B. *Environ. Sci.: Atmos.* **2025**, *5*, 530–534.

[25] Pérez-Peña, M. P.; Fisher, J. A.; Hansen, C.; Kable, S. H. Reply to the 'Comment on "Assessing the atmospheric fate of trifluoroacetaldehyde (CF_3CHO) and its potential as a new source of fluoroform (HFC-23) using the AtChem2 box model"' by O. J. Nielsen, M. P. Sulbaek Andersen and J. Franklin, Environ. Sci.: Atmos., 2025, 5, DOI: 10.1039/D4EA00123K. *Environmental Science: Atmospheres* **2025**, *5*, 535–538.

[26] Antiñolo, M.; Bravo, I.; Jim´enez, E.; Ballesteros, B.; Albaladejo, J. Atmospheric Chemistry of E- and Z-CF_3CH – CHF (HFO-1234ze): OH Reaction Kinetics as a Function of Temperature and UV and IR Absorption Cross Sections. *The Journal of Physical Chemistry A* **2017**, *121*, 8322–8331, PMID: 28992690.

[27] Calvert, J.; Mellouki, A.; Orlando, J.; Pilling, M.; Wallington, T. *Mechanisms of Atmospheric Oxidation of the Oxygenates*; Oxford University Press, 2011.

[28] Chiappero, M. S.; Malanca, F. E.; Argüello, G. A.; Wooldridge, S. T.; Hurley, M. D.; Ball, J. C.; Wallington, T. J.; Waterland, R. L.; Buck, R. C. Atmospheric Chemistry of Perfluoroaldehydes ($CxF_2x+1CHO$) and Fluorotelomer Aldehydes ($CxF_2x+1\ CH_2CHO$): Quantification of the Important Role of Photolysis. *The Journal of Physical Chemistry A* **2006**, *110*, 11944–11953, PMID: 17064182.

[29] Bohnenstengel, S. I. et al. Meteorology, Air Quality, and Health in London: The ClearfLo Project. *Bulletin of the American Meteorological Society* **2015**, *96*, 779 – 804.

[30] Bey, I.; Jacob, D. J.; Yantosca, R. M.; Logan, J. A.; Field, B. D.; Fiore, A. M.; Li, Q.; Liu, H. Y.; Mickley, L. J.; Schultz, M. G. Global modeling of tropospheric chemistry with assimilated meteorology: Model description and evaluation. *Journal of Geophysical Research: Atmospheres* **2001**, *106*, 23072–23095.

[31] Jacob, D. J. *Introduction to Atmospheric Chemistry*; Princeton University Press: Princeton, 1999.

[32] Brasseur, G. P.; Jacob, D. J. *Modeling of Atmospheric Chemistry* ; Cambridge University Press: Cambridge, 2017.

View Article Online
DOI: 10.1039/D6EA00034G

[33] Wu, S.; Mickley, L. J.; Jacob, D. J.; Logan, J. A.; Yantosca, R. M.; Rind, D. Why are there large differences between models in global budgets of tropospheric ozone? *Journal of Geophysical Research: Atmospheres* **2007**, *112* .

[34] Lin, H.; Jacob, D. J.; Lundgren, E. W.; Sulprizio, M. P.; Keller, C. A.; Fritz, T. M.; Eastham, S. D.; Emmons, L. K.; Campbell, P. C.; Baker, B.; Saylor, R. D.; Montuoro, R. Harmonized Emissions Component (HEMCO) 3.0 as a versatile emissions component for atmospheric models: application in the GEOS-Chem, NASA GEOS, WRF-GC, CESM2, NOAA GEFS-Aerosol, and NOAA UFS models. *Geoscientific Model Development* **2021**, *14*, 5487–5506.

[35] Hoesly, R. M. et al. Historical (1750–2014) anthropogenic emissions of reactive gases and aerosols from the Community Emissions Data System (CEDS). *Geoscientific Model Development* **2018**, *11*, 369–408.

[36] Randerson, J. T.; van der Werf, G. R.; Giglio, L.; Collatz, G. J.; Kasibhatla, P. S. Global Fire Emissions Database, Version 4.1 (GFEDv4). 2017; https://doi.org/10.3334/ORNLDAAC/1293, Date Accessed: 2025-09-25.

[37] Guenther, A. B.; Jiang, X.; Heald, C. L.; Sakulyanontvittaya, T.; Duhl, T.; Emmons, L. K.; Wang, X. The Model of Emissions of Gases and Aerosols from Nature version 2.1 (MEGAN2.1): an extended and updated framework for modeling biogenic emissions. *Geoscientific Model Development* **2012**, *5*, 1471–1492.

[38] Rusch, G. M. The development of environmentally acceptable fluorocarbons. *Critical Reviews in Toxicology* **2018**, *48*, 615–665.

[39] Center for International Earth Science Information Network – CIESIN – Columbia University Gridded Population of the World, Version 4 (GPWv4): Population Density, Revision 11. 2018.

[40] Montzka, S. A.; Burkholder, J. B. *Report of the Scientific Assessment Panel in response to Decision XXXV/7: Emissions of HFC-23* ; UNEP Report, 2024; Prepared for the Meeting of the Parties to the Montreal Protocol.

[41] Sulbaek Andersen, M. P.; Madronich, S.; Ohide, J. M.; Frausig, M.; Nielsen, O. J. Photolysis of CF_3CHO at 254 nm and potential contribution to the atmospheric abundance of HFC-23. *Atmospheric Environment* **2023**, *314*, 120087.

[42] Vollmer, M. K.; Reimann, S.; Hill, M.; Brunner, D. Update to: First Observations of the Fourth Generation Synthetic Halocarbons HFC-1234yf, HFC-1234ze(E), and HCFC-1233zd(E) in the Atmosphere. *Environmental Science & Technology* **2015**, *49*, 2703–2708, PMID: 25625175.

View Article Online
DOI: 10.1039/D6EA00034G

[43] Vollmer, M. K. et al. Global Observations and European emissions of the halogenated olefins HFO-1234yf, HFO-1234ze(E), and HCFO-1233zd(E) from the AGAGE (Advanced Global Atmospheric Gases Experiment) network. *EGUsphere* **2025**, *2025*, 1–46.

[44] Crippa, M. et al. EDGAR - Emissions Database for Global Atmospheric Research, release EDGAR 2024 GHG (1970–2023). https://edgar.jrc.ec.europa.eu/dataset_ghg2024, 2023; Pub-lications Office of the European Union, Luxembourg, doi:10.2760/4002897.

[45] van Caspel, W. E.; Simpson, D.; Jonson, J. E.; Benedictow, A. M. K.; Ge, Y.; di Sarra, A.; Pace, G.; Vieno, M.; Walker, H. L.; Heal, M. R. Implementation and evaluation of updated photolysis rates in the EMEP MSC-W chemistry-transport model using Cloud-J v7.3e. *Geoscientific Model Development* **2023**, *16*, 7433–7459.

[46] Burkholder, J. B.; Sander, S. P.; Abbatt, J. P. D.; Barker, J. R.; Cappa, C.; Crounse, J. D.; Dib-ble, T. S.; Huie, R. E.; Kolb, C. E.; Kurylo, M. J.; Orkin, V. L.; C. Percival, J.; Wilmouth, D. M.; Wine, P. H. *Chemical Kinetics and Photochemical Data for Use in Atmospheric Studies: Evaluation Number 19* ; National Aeronautics and Space Administration, Jet Propulsion Laboratory, California Institute of Technology: Pasadena, California, 2020.

[47] Damian, V.; Sandu, A.; Damian, M.; Potra, F.; Carmichael, G. R. The kinetic preprocessor KPP-a software environment for solving chemical kinetics. *Computers and Chemical Engineering* **2002**, *26*, 1567–1579.

[48] Baumann, F.; Fernholz, C.; Lelieveld, J.; Crowley, J. N. Kinetics of the reaction of CF_3CHO with OH between 204 K and 361 K. *Phys. Chem. Chem. Phys.* **2025**, *27*, 18907–18916.

[49] Wesely, M. L. Parameterization of surface resistances to gaseous dry deposition in regional-scale numer-ical models. *Atmospheric Environment* **1989**, *23*, 1293–1304.

[50] Liu, H.; Jacob, D. J.; Bey, I.; Yantosca, R. M. Constraints from 210Pb and 7Be on wet deposition and transport in a global three-dimensional chemical tracer model driven by assimilated meteorological fields. *Journal of Geophysical Research: Atmospheres* **2001**, *106*, 12109–12128.

[51] Bi, C.; Isaacman-VanWertz, G. Estimated timescales for wet deposition of organic compounds as a function of Henry's law constants. *Environ. Sci.: Atmos.* **2022**, *2*, 1526–1533.

[52] China Meteorological Association China Meteorological Association - Climate Data Center. 2014; https: //web.archive.org/web/20140727001008/http://cdc.cma.gov.cn/cdc_en/home.dd, Archived ver-sion, accessed: 28-Jan-2025.

[53] Porter, W. C.; Heald, C. L. The mechanisms and meteorological drivers of the summertime ozone–temperature relationship. *Atmospheric Chemistry and Physics* **2019**, *19*, 13367–13381.

View Article Online
DOI: 10.1039/D6EA00034G

[54] Kavassalis, S. C.; Murphy, J. G. Understanding ozone-meteorology correlations: A role for dry deposition. *Geophysical Research Letters* **2017**, *44*, 2922–2931.

[55] Prinn, R. G. et al. History of Chemically and Radiatively Important Atmospheric Gases from the Advanced Global Atmospheric Gases Experiment (AGAGE). *Earth System Science Data* **2018**, *10*, 985–1018.

[56] Prinn, R. G. et al. A history of chemically and radiatively important gases in air deduced from ALE/GAGE/AGAGE. *Journal of Geophysical Research: Atmospheres* **2000**, *105*, 17751–17792.

[57] Reimann, S.; Schaub, D.; Stemmler, K.; Folini, D.; Hill, M.; Hofer, P.; Buchmann, B.; Simmonds, P. G.; Greally, B. R.; O'Doherty, S. Halogenated greenhouse gases at the Swiss High Alpine Site of Jungfraujoch (3580 m asl): Continuous measurements and their use for regional European source allocation. *Journal of Geophysical Research: Atmospheres* **2004**, *109*, D05307.

[58] Kim, J.; Lee, J.; Choi, S.-D.; Kim, Y.; Ghim, Y. Gaseous and particulate polycyclic aromatic hydrocarbons at the Gosan background site in East Asia. *Atmospheric Environment* **2012**, *49*, 311–319.

[59] Platt, S. M. et al. Atmospheric composition in the European Arctic and 30 years of the Zeppelin Observatory, Ny-Ålesund. *Atmospheric Chemistry and Physics* **2022**, *22*, 3321–3369.

[60] Eckhardt, S.; Stohl, A.; Beirle, S.; Spichtinger, N.; James, P.; Forster, C.; Junker, C.; Wagner, T.; Platt, U.; Jennings, S. G. The North Atlantic Oscillation controls air pollution transport to the Arctic. *Atmospheric Chemistry and Physics* **2003**, *3*, 1769–1778.

[61] Patra, P. K. et al. TransCom model simulations of CH4 and related species: linking transport, surface flux and chemical loss with CH4 variability in the troposphere and lower stratosphere. *Atmospheric Chemistry and Physics* **2011**, *11*.

[62] Hossaini, R.; Chipperfield, M. P.; Saiz-Lopez, A.; Fernandez, R.; Monks, S.; Feng, W.; Brauer, P.; von Glasow, R. A global model of tropospheric chlorine chemistry: Organic versus inorganic sources and impact on methane oxidation. *Journal of Geophysical Research: Atmospheres* **2016**, *121*, 14,271–14,297.

[63] Stanley, K. M.; Say, D.; Mühle, J.; Harth, C. M.; Krummel, P. B.; Young, D.; O'Doherty, S. J.; Salameh, P. K.; Simmonds, P. G.; Weiss, R. F.; Prinn, R. G.; Fraser, P. J.; Rigby, M. Increase in global emissions of HFC-23 despite near-total expected reductions. *Nature Communications* **2020**, *11*, 397.

[64] Wang, Y.; Liu, L.; Qiao, X.; Sun, M.; Guo, J.; Zhang, J.; Zhao, B. Projections of National-Gridded Emissions of Hydrofluoroolefins (HFOs) in China. *Environmental Science & Technology* **2023**, *57*, 8650–8659, PMID: 37235871.

View Article Online
DOI: 10.1039/D6EA00034G

[65] European Commission Regulation (EU) 2024/573 of the European Parliament and of the Council of 7 February 2024 on fluorinated greenhouse gases. Official Journal of the European Union, L 759, 1–76, 2024; https://eur-lex.europa.eu/legal-content/EN/TXT/?uri=CELEX%3A32024R0573.

[66] United States Congress American Innovation and Manufacturing Act of 2020. Public Law No: 116-260, Division S, Title VI, 2020; https://www.congress.gov/bill/116th-congress/senate-bill/2754.

[67] Lu, Y.; Khalil, M. Tropospheric OH: model calculations of spatial, temporal, and secular variations. *Chemosphere* **1991**, *23*, 397–444.

[68] Malashock, D. A.; Delang, M. N.; Becker, J. S.; Serre, M. L.; West, J. J.; Chang, K.; Cooper, O. R.; Anenberg, S. C. Estimates of ozone concentrations and attributable mortality in urban, peri-urban and rural areas worldwide in 2019. *Environmental Research Letters* **2022**, *17*, 958–967.

[69] Saunders, S. M.; Jenkin, M. E.; Derwent, R. G.; Pilling, M. J. Protocol for the development of the Master Chemical Mechanism, MCM v3 (Part A): tropospheric degradation of non-aromatic volatile organic compounds. *Atmospheric Chemistry and Physics* **2003**, *3*, 161–180.

[70] Hodnebrog, Ø.; Etminan, M.; Fuglestvedt, J. S.; Marston, G.; Myhre, G.; Nielsen, C. J.; Shine, K. P.; Wallington, T. J. Global warming potentials and radiative efficiencies of halocarbons and related compounds: A comprehensive review. *Reviews of Geophysics* **2013**, *51*, 300–378.

[71] Scheurer, M.; Nödler, K.; Freeling, F.; Janda, J. J.; Happel, O.; Riegel, M.; Müller, U.; Rüdiger Storck, F.; Fleig, M.; Lange, F. T.; Brunsch, A.; Brauch, H.-J. Small, mobile, persistent: Trifluoroacetate in the water cycle – Overlooked sources, pathways, and consequences for drinking water supply. *Water Research* **2017**, *126*, 460–471.

[72] Freeling, F.; Björnsdotter, M. K. Assessing the environmental occurrence of the anthropogenic contaminant trifluoroacetic acid (TFA). *Current Opinion in Green and Sustainable Chemistry* **2023**, *41*, 100807.

[73] Sulbaek Andersen, M. P.; Toft, A.; Nielsen, O. J.; Hurley, M. D.; Wallington, T. J.; Chishima, H.; Tonokura, K.; Mabury, S. A.; Martin, J. W.; Ellis, D. A. Atmospheric Chemistry of Perfluorinated Aldehyde Hydrates (n-$C_xF_{2x+1}CH(OH)_2$, x = 1, 3, 4): Hydration, Dehydration, and Kinetics and Mechanism of Cl Atom and OH Radical Initiated Oxidation. *The Journal of Physical Chemistry A* **2006**, *110*, 9854–9860, PMID: 16898686.

[74] Hart, L. et al. Growth in Production and Environmental Deposition of Trifluoroacetic Acid Due To Long-Lived CFC Replacements and Anesthetics. *Geophysical Research Letters* **2026**, *53*, e2025GL119216.

View Article Online
DOI: 10.1039/D6EA00034G

Data Availability

Observational data for HFO-1234ze(E) were obtained from the Advanced Global Atmospheric Gases Experiment (AGAGE) network. AGAGE data are available from

https://doi.org/10.5194/egusphere-2025-4824. GEOS-Chem model configuration files and emissions inventories are available at https://github.com/bethkillen. GEOS-Chem (https://geos-chem.readthedocs.io/en/stable/) and AtChem2 (https://github.com/AtChem/AtChem2) are open-source software. The full model output is available on request.